Relating influenza virus membrane fusion kinetics to stoichiometry of neutralizing antibodies at the single-particle level

Jason J. Otterstrom[a,b,1], Boerries Brandenburg[c], Martin H. Koldijk[c], Jarek Juraszek[c], Chan Tang[c], Samaneh Mashaghi[b], Ted Kwaks[c], Jaap Goudsmit[c], Ronald Vogels[c], Robert H. E. Friesen[c], and Antoine M. van Oijen[b,2]

[a]Harvard University Biophysics Program, Harvard Medical School, Boston, MA 02115; [b]Centre for Synthetic Biology, Zernike Institute for Advanced Materials, University of Groningen, 9747 AG, Groningen, The Netherlands; and [c]Crucell Vaccine Institute, Janssen Center of Excellence for Immunoprophylaxis, 2333 CN, Leiden, The Netherlands

Edited by Robert A. Lamb, Northwestern University, Evanston, IL, and approved October 21, 2014 (received for review June 23, 2014)

The ability of antibodies binding the influenza hemagglutinin (HA) protein to neutralize viral infectivity is of key importance in the design of next-generation vaccines and for prophylactic and therapeutic use. The two antibodies CR6261 and CR8020 have recently been shown to efficiently neutralize influenza A infection by binding to and inhibiting the influenza A HA protein that is responsible for membrane fusion in the early steps of viral infection. Here, we use single-particle fluorescence microscopy to correlate the number of antibodies or antibody fragments (Fab) bound to an individual virion with the capacity of the same virus particle to undergo membrane fusion. To this end, individual, infectious virus particles bound by fluorescently labeled antibodies/Fab are visualized as they fuse to a planar, supported lipid bilayer. The fluorescence intensity arising from the virus-bound antibodies/Fab is used to determine the number of molecules attached to viral HA while a fluorescent marker in the viral membrane is used to simultaneously obtain kinetic information on the fusion process. We experimentally determine that the stoichiometry required for fusion inhibition by both antibody and Fab leaves large numbers of unbound HA epitopes on the viral surface. Kinetic measurements of the fusion process reveal that those few particles capable of fusion at high antibody/Fab coverage display significantly slower hemifusion kinetics. Overall, our results support a membrane fusion mechanism requiring the stochastic, coordinated action of multiple HA trimers and a model of fusion inhibition by stem-binding antibodies through disruption of this coordinated action.

influenza | neutralizing antibody | hemagglutinin | neutralization stoichiometry | membrane fusion

Recently described antibodies capable of neutralizing a broad range of influenza viruses through recognition of highly conserved epitopes on the hemagglutinin protein (HA) have potential use as antiinfluenza therapeutics and for rational design of vaccines, HA-binding proteins, and small molecules (1–5). Such diverse applications require a detailed understanding of the infection mechanisms that are disrupted by antibody binding. An important parameter for in vitro antibody characterization is the binding stoichiometry, which relates the number of antibodies that must bind a virus in order to achieve a functional output, such as viral neutralization (6, 7). Here, we use fluorescence microscopy to visualize individual virus particles and measure the stoichiometry of broadly neutralizing antibodies as they disrupt the fusogenic activity of the HA protein.

The homotrimeric HA transmembrane protein consists of two disulfide-linked domains, HA1 and HA2 (8, 9), and exhibits substantial antigenic drift, having two phylogenetically distinct groups—groups 1 and 2—with 18 subtypes (10). The HA1 head domain, distal from the viral envelope, contains a binding site for sialic acid moieties that binds virions to a target cell and facilitates their entry into a cellular endosome via clathrin-mediated endocytosis. The HA2 stem domain comprises mostly the envelope-proximal ectodomain and the transmembrane domain. The low pH of late endosomes triggers the stem to unfold and embed its hydrophobic N-terminal region into the endosomal membrane. Refolding of the protein brings the viral and endosomal membranes close together and catalyzes their fusion (11, 12). Several biophysical studies indicate that multiple HA trimers must work together by coordinating their conformational changes for membrane fusion to occur (13–16).

Head-binding antibodies typically recognize variable loop regions surrounding the receptor site and show serotype-specific neutralization (1, 17, 18), although some can neutralize a limited set of viral serotypes (19–21). In contrast, stem-binding antibodies recognize an epitope region that is highly conserved between influenza strains and possess a broad neutralization capacity across many viral subtypes (19, 22–26) or even across groups (19, 27, 28). We recently demonstrated that binding of HA by the broadly neutralizing, stem-binding antibodies CR6261 (group 1-specific) and CR8020 (group 2-specific) (22–24) results in inhibition of HA-mediated viral membrane fusion (29). The ability of antibodies to block fusion confirms the accessibility of their membrane-proximal epitope on intact viruses despite the dense packing of surface proteins (Fig. 1*A*), an aspect also recently shown by cryoelectron tomography (30).

Significance

We determine the number of broadly neutralizing antibodies required to inhibit influenza virus membrane fusion by simultaneously observing individual viral particles undergoing fusion and counting the number of antibodies bound to them. The viral membrane fusion process is mediated by fusion proteins whose activity is blocked through the binding of these antibodies to evolutionarily conserved epitopes. Surprisingly, the number of antibodies required for inhibition is markedly lower than the number of fusion proteins present, indicating virus neutralization does not require saturation of epitope occupancy. Overall, our results support a model of membrane fusion requiring several fusion proteins working together in a coordinated, stochastic fashion, and the inhibition of this process through disruption of fusion protein coordination.

Author contributions: J.J.O., B.B., R.H.E.F., and A.M.v.O. designed research; J.J.O. and J.J. performed research; B.B., C.T., S.M., T.K., J.G., R.V., and R.H.E.F. contributed new reagents/analytic tools; B.B., T.K., J.G., R.V., and R.H.E.F. contributed broadly neutralizing antibodies; S.M. contributed PEG-surface functionalization; J.J.O., M.H.K., and J.J. analyzed data; and J.J.O., B.B., R.H.E.F., and A.M.v.O. wrote the paper.

Conflict of interest statement: B.B., M.H.K., J.J., C.T., T.K., J.G., R.V., and R.H.E.F. are current employees of the Crucell Vaccine Institute.

This article is a PNAS Direct Submission.

[1]Present address: ICFO-The Institute of Photonic Sciences, 08860 Castelldefels, Spain.

[2]To whom correspondence should be addressed. Email: a.m.van.oijen@rug.nl.

This article contains supporting information online at www.pnas.org/lookup/suppl/doi:10.1073/pnas.1411755111/-/DCSupplemental.

Radioisotope labeling of neutralizing IgG antibodies previously indicated that neutralization stoichiometries required large numbers of epitopes to be bound (18, 31). These results were in line with multihit and coating models of virus neutralization, as opposed to single-hit models involving a critical site vulnerable to neutralization (6, 32, 33). However, such experiments are complicated by a convolution of cell-binding inhibition, inhibition of membrane fusion, aggregation of virus particles, and the abrogation of infection postentry (18, 33).

Here, we use a novel fluorescence imaging approach to simultaneously quantify the number of CR6261 or CR8020 antibodies (IgG) or their Fab-fragments (Fab) bound to an individual, infectious virus while directly visualizing its capacity for membrane fusion. This measurement strategy allows us to directly correlate binding stoichiometry to its functional effect of inhibiting HA-mediated membrane fusion. We find that a virus can be rendered nonfusogenic while still having large numbers of unbound HA epitopes. Furthermore, binding of the neutralizing IgG/Fab molecules causes a delay in the kinetics of membrane fusion. Our methodology provides insight into the mechanism of HA-mediated fusion that is difficult to obtain via conventional approaches (34).

Results

Fluorescently Labeled IgG and Fab Inhibit Hemifusion. We observed individual influenza virus particles by labeling their envelope with the lipophilic dye R18 at concentrations causing partial self-quenching of the dye's fluorescence. We have previously confirmed that the viruses maintain their infectivity following R18 labeling (29). R18-labeled viruses (A/Puerto Rico/8/34 H1N1 or A/Aichi/68-X31 H3N2) were incubated with the broadly neutralizing, stem-binding antibodies CR6261 or CR8020 (collectively IgG), or their Fab fragments (crF6261 or crF8020, respectively), at increasing concentrations before immobilization. We immobilized the viruses on a planar, lipid bilayer that is formed on top of a glass microscope coverslip placed on an inverted fluorescence microscope (Fig. 1*B*). Incubation conditions ensured that IgG/Fab binding had achieved equilibrium before immobilization, and dissociation over the course of the experiment was found to be negligible (Fig. S1). One hundred or more virus particles per ~140×70-μm^2 field of view were capable of binding to the glass-supported bilayers even at IgG/Fab concentrations as high as 1 μM (Fig. S2). After lowering the pH, we visualize influenza HA-mediated hemifusion of the viral envelope with the bilayer through R18 dequenching at the site of each virus particle (Fig. 1 *C* and *D* and refs. 15, 16, and 29). We quantify the hemifusion efficiency as the ratio of virions that underwent fusion to the total number of viral particles visualized. Data in Fig. 2*A* demonstrates that binding of Alexa Fluor 488-labeled IgG (5.4 ± 0.8 dyes/CR6261 IgG and 5.0 ± 0.5 dyes/CR8020 IgG; Fig. S3 and Table S1) or Fab (2.4 ± 0.3 dyes/crF6261 Fab and 2.3 ± 0.1 dyes/crF8020 Fab) to viral HA causes a group-specific, dose-dependent reduction in the hemifusion efficiency of the H1N1 and H3N2 viral strains, similar to our previous reports (29). This observation indicates that both monovalent and bivalent binding (valency referring to the number of paratopes

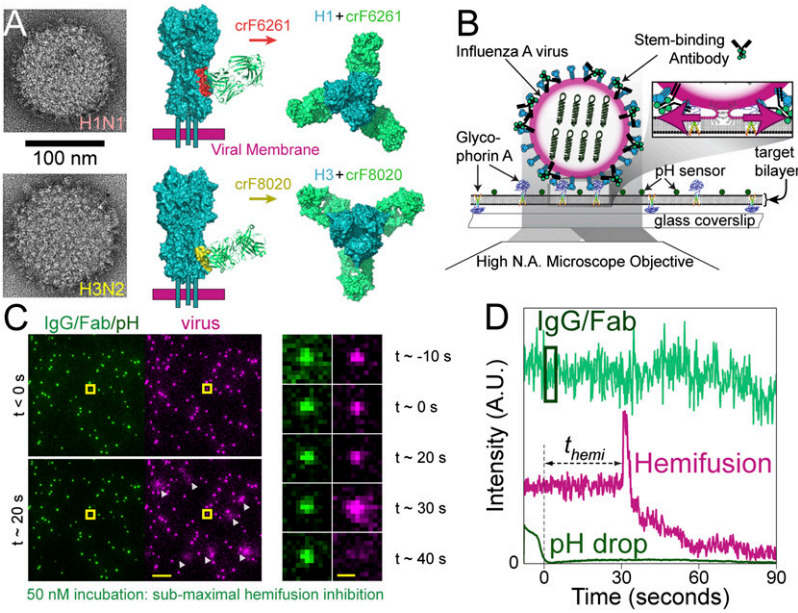

Fig. 1. Experimental design and readouts. (*A*, *Left*) Transmission EM images of the two influenza A viruses, H1N1 (*Top*) and H3N2 (*Bottom*), depicting the high density of spike proteins present on the viral surface. (*A*, *Middle* and *Left*) Side and top views, respectively, showing a space-filling model of crF6261 bound to H1 [*Top*, Protein Data Bank (PDB) ID code 3GBN with epitope in red] and crF8020 bound to H3 (*Bottom*, PDB ID code 3SDY with epitope in yellow). These crystal structures highlight differences in proximity of the two epitopes to the viral membrane and of the HA–Fab angle upon binding. (*B*) Schematic depiction of experimental design. Alexa-488–labeled IgG (or Fab) are bound to R18-labeled influenza A viruses (magenta-edged sphere) immobilized on a glass-supported planar bilayer through interaction with glycophorin A; pH-sensitive fluorescein (pK_a 6.4) is also bound to the bilayer surface. Fluorescence is excited and detected via objective TIRF microscopy. Zoom: Acidification of the virus particles causes membrane fusion, resulting in escape of the R18 dye from the viral membrane into the target bilayer and producing a dequenching signal. (*C*, *Left*) False-color still frames from a fusion movie at time points before (*Top*) and 20 s after (*Bottom*) the pH drop. (Scale bar: 10 μm.) IgG/Fab (green spots, 50 nM incubation) and fluorescein (diffuse background) are visualized on the left, whereas the R18-labeled viruses (magenta) and their low pH-induced dequenching (white triangles) are simultaneously visualized on the right. (*C*, *Right*) Image montage of the virus highlighted by the yellow square, which is covered with a subinhibitory number of IgG molecules (green). Its fusion to the bilayer is seen as a flash of R18 intensity (magenta) followed by outward R18 diffusion. (Scale bar: 1 μm.) (*D*) Fluorescence time trajectory for the highlighted virus in *C*. Time $t = 0$ is set to loss of the fluorescein signal (dark green) upon arrival of the fusion-inducing pH 5.0 buffer. The time to hemifusion, t_{hemi}, occurs at $t \approx$ 30 s for this virus particle and is observed as the abrupt increase in R18 fluorescence (magenta). The virus-bound IgG/Fab fluorescence (light green) used for stoichiometry measurements is indicated by the box: 1 s after the pH drop and enclosing 3 s of fluorescence information.

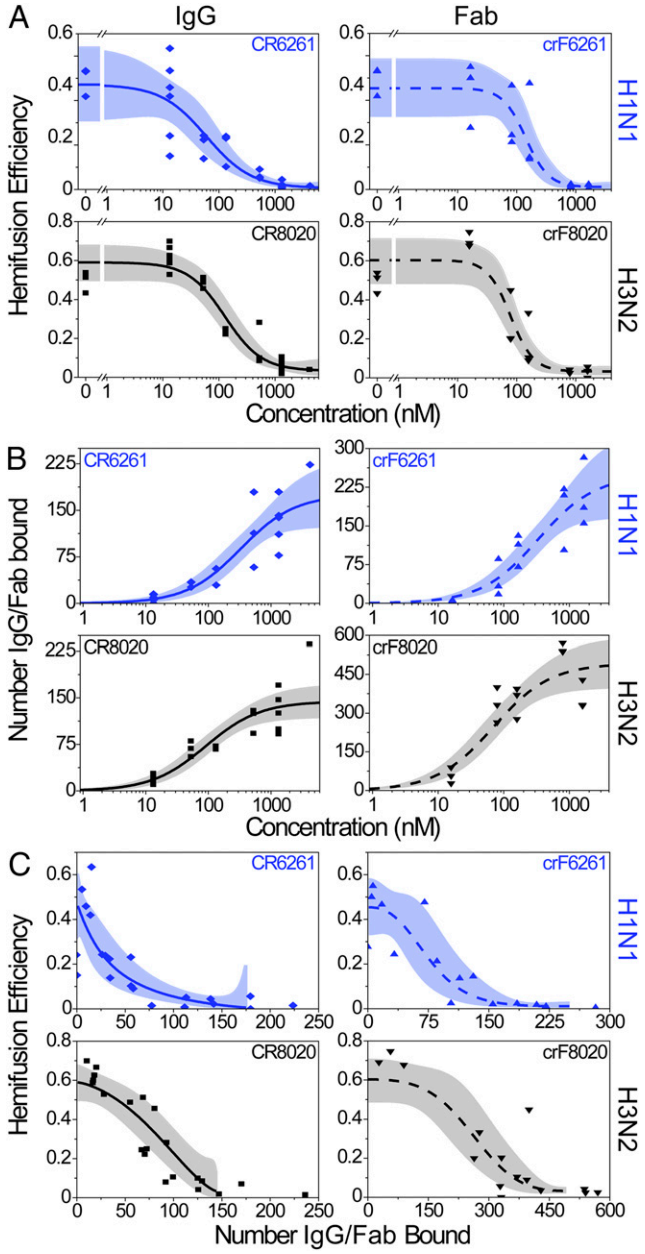

Fig. 2. Hemifusion inhibition and antibody stoichiometry. In *A–C*, IgG data are on the left-hand graphs (solid fit lines), Fab data are on the right (dashed fit lines); top rows are the H1N1 strain (blue) and bottom rows are H3N2 (black). Each data point represents a single experimental run (CR6261 IgG shown as diamonds, crF6261 Fab as upward triangles, CR8020 IgG as squares, and crF8020 as downward triangles); the best-fit lines are in blue or black and their 95% confidence bands are in light blue or gray. (*A*) Hemifusion efficiency decreases as the concentration of neutralizing IgG or Fab is increased. (*B*) The median number of neutralizing IgG or Fab bound to virions increases as the concentration used for incubation with virus increases. (*C*) Plot of hemifusion data (*A*) versus the number of IgG or Fab bound to the viral surface (*B*), allowing for the estimation of the number of IgG/Fab required for a given reduction in hemifusion efficiency. Fit lines used are the logistic function (*A*), hyperbolic function (*B*), and a combination of the two (*C*) (*SI Materials and Methods*). Fit lines in *C* are truncated at high coverage and correspond to the plateau values obtained in *A* and *B* at high IgG/Fab concentrations.

bound to epitopes) can lead to hemifusion inhibition directly through epitope recognition.

Using bilayers supported by a PEG or dextran cushion (15) (rather than by glass), we were able to observe viral content release and found that the requisite formation of a fusion pore was inhibited to a similar extent as hemifusion, indicating that hemifusion is, indeed, a functional readout for full fusion (Fig. S4). In a few instances at low IgG concentration, antibody-labeled hemagglutinin proteins could be seen to diffuse into the target bilayer after successful content release (Movies S1–S3). This observation demonstrates a complete merger of the viral membrane with the target-supported bilayer.

Maximal Hemifusion Inhibition by IgG Binding Occurs Below Full Epitope Occupancy. Binding stoichiometry for each virus particle is determined as a quotient of two integrated fluorescence intensity measurements: intensity from IgG/Fab bound to a virus (Fig. 1), I_{bound}, and intensity from individual IgG/Fab molecules, $I_{\text{individual}}$. The latter is measured by visualizing individual, labeled IgG/Fab molecules under identical illumination conditions in the absence of virus and target bilayer (Fig. S5). The number of molecules bound to an individual virion is calculated as $N_{\text{bound}} = I_{\text{bound}}/I_{\text{individual}}$. IgG/Fab detection efficiency was >99% for IgG and ~90% for Fab (Table S1), and reported numbers of bound IgG/Fab were corrected for the small amounts of unlabeled molecules.

The median number of IgG/Fab bound to individual virions for each experiment performed is presented in Fig. 2*B*. Upon increasing IgG/Fab concentrations, the number of IgG/Fab molecules bound to a virus (fusing and nonfusing) increases sigmoidally, with the upper plateau corresponding to the region of Fig. 2*A* where the hemifusion efficiency is zero. Hence, this plateau value provides an estimate for the number of IgG/Fab molecules that must bind a virus to achieve maximum inhibition of hemifusion. This upper limit (asymptote) does not correspond to saturation of epitope binding, which we were not able to ascertain experimentally due to technical limitations of achievable labeled antibody concentrations and of required virus concentrations (*SI Materials and Methods*). Moreover, virus saturation by antibody binding occurs at higher concentrations than those required for neutralization in viral neutralization assays (VNAs) (18). Rather, the upper limit more relevantly reports the functional outcome of epitope binding, namely hemifusion inhibition, and the number of IgG/Fab needed to cause it. These and other stoichiometric values are summarized in Table 1, with calculated fit parameters reported in Table S2, including the 95% confidence intervals.

Under conditions of maximum hemifusion inhibition, we find that both viral strains are bound by comparable numbers of IgG molecules (175 for H1N1 and 144 for H3N2), whereas there is a difference in the number of Fab bound (248 for H1N1 and 493 for H3N2). Rationales for this difference are considered in *Discussion*. At the highest IgG concentrations we could achieve, ~4,200 nM, we observed full hemifusion inhibition and measured 224 CR6261 IgG and 236 CR8020 IgG bound to the H1N1 and H3N2 viruses, respectively. Thereby, we show that more stem-binding IgG can sterically fit on the surface of hemifusion-inhibited virions than what is required for maximal inhibition.

To gain insight into the mechanism of hemifusion inhibition through IgG/Fab binding, we first compared the number bound at maximum hemifusion inhibition to estimates of the number of HA trimers on the viral surface. Previous studies have estimated 300–500 HA trimers per 120-nm diameter spherical virion (35–37), a size comparable to our viral strains (125 nm diameter, Fig. S6). Concordantly, recent cryoelectron tomography reconstruction of viruses produced identically to those that we have used (30, 38) indicate there are ~375 HA trimers on each virus. Using this estimate and the data for the maximum fusion inhibition (Table 1) we calculate an IgG:HA stoichiometry of 0.47 and 0.38 for CR6261 and CR8020 IgG, respectively. For the Fab we estimate a Fab:HA stoichiometry of 0.69 and 1.31 for crF6261 and crF8020, respectively. These observations are consistent with predictions that the larger, bivalent IgG molecules would have lower stoichiometries relative to the smaller, monovalent Fab (30). For

Table 1. Summary of stoichiometric and kinetic results

Virus	Neutralizing molecule	IgG/Fab bound at maximum hemifusion inhibition	IgG/Fab bound at half-maximum hemifusion inhibition	Fractional occupancy at half-maximum inhibition*	Fold increase of hemifusion time
H1N1	CR6261 IgG	175 (122–229)	27 (6–65)	0.16 (0.03–0.39)	2.2 (1.6–3.0)
	crF6261 Fab	248 (158–338)	74 (39–119)	0.30 (0.12–0.55)	2.7 (1.6–4.5)
H3N2	CR8020 IgG	144 (119–170)	84 (62–110)	0.59 (0.41–0.79)	2.1 (1.5–2.9)
	crF8020 Fab	493 (394–592)	261 (192–340)	0.53 (0.36–0.73)	2.6 (2.2–3.0)

Values in parenthesis report 95% confidence intervals.
*Quotient of IgG/Fab bound at half-maximum and maximum hemifusion inhibition.

the IgG specifically, stoichiometry values less than one indicate that not every HA trimer needs an IgG bound for hemifusion to be inhibited and suggests that bivalent binding may play a role in hemifusion inhibition.

Secondly, we investigated steric interactions on the viral surface and binding valency in silico through a coarse-grained 2D Monte Carlo simulation (*SI Materials and Methods*) of protein packing. Thousands of random, viral surfaces with dense protein packing were generated using the crystallographic dimensions of the envelope proteins (HA, neuraminidase, and M2 proton channel) at appropriate relative concentrations. Surface density was set to mimic a viral surface having 375 HA trimers, then increasing numbers of IgG/Fab were bound to HA in accord with their cocrystal structure (23, 24). The number of IgG/Fab bound when overlap between neighboring proteins could no longer be prevented was taken as the sterically allowed maximum.

Simulations indicated that a maximum of 270–300 IgG sterically fit on a viral surface (Fig. S7). These values are in agreement with 3D cryo-EM results that steric interactions alone permit 75% of the 375 HA to complex with IgG (30). Our simulations revealed that bivalent IgG binding would prevail until ∼175 IgG molecules had bound, at which point monovalent binding would become dominant (Fig. S7). This result suggests that the 175 CR6261 or 144 CR8020 IgG bound at maximum hemifusion inhibition (Table 1) would bind bivalently to abrogate the fusogenicity of up to 350 or 288 HA trimers, respectively. These numbers are lower than estimates for the total number of HA trimers present on a virus and substantially lower than the number of epitopes present on a virus. Our simulations predict that ∼500 Fab molecules could fit on a virus (Fig. S7), although no previous predictions have been made for the number of Fab that could bind a virus. This steric maximum agrees with the experimentally determined number of crF8020, however, only about half as many crF6261 bind at maximum hemifusion inhibition. Overall, we conclude that not all sterically available epitopes need to be bound by IgG/Fab for the membrane fusion capacity of a virus particle to be blocked.

Low Occupancies Can Significantly Reduce the Extent of Hemifusion. Combining measurements of hemifusion efficiency with the number of virus-bound IgG/Fab molecules (Fig. 2*C*; see *SI Materials and Methods* for data fitting) allows us to calculate the number of IgG/Fab molecules needed to reduce hemifusion efficiency by half. Such a value is akin to an EC_{50}, but is a direct measurement of the number of virus-bound IgG/Fab causing the reduction in hemifusion efficiency rather than reporting a concentration. For example, we calculate that 27 CR6261 IgG need to bind the H1N1 virus for the hemifusion efficiency to be reduced 50% from 0.47 to 0.24 (Fig. 2*C*). Results of these calculations are listed in Table 1.

We next define the fractional occupancy as the ratio of the number of IgG/Fab bound at half-maximum hemifusion inhibition to the number of IgG/Fab bound at maximum hemifusion inhibition. For H1N1 at half-maximum hemifusion inhibition, the fractional occupancy is 27/175 = 0.16 (Table 1). This definition focuses on the functional consequence of IgG/Fab binding by defining it relative to the number of occupied binding sites required for maximum hemifusion inhibition rather than the number of sterically available sites. Fig. 2*C* and Table 1 show that fractional occupancy significantly lower than unity leads to half-maximum hemifusion inhibition. Comparing the fractional occupancies, we find that they are similar for the IgG and Fab of both 6261 and 8020, respectively. We also detect a difference in the fractional occupancy between the two viral strains being bound by the two IgG/Fab used in our experiments.

IgG/Fab Binding Delays the Time to Hemifusion. The time to hemifusion is measured as the time between disappearance of the fluorescein signal (pH drop) and the onset of dequenching caused by lipophilic dye escape from the site of viral fusion (Fig. 1*C*). Concurrent with decreasing hemifusion efficiency and increasing numbers of bound IgG/Fab, Fig. 3 shows that the time required for the remaining fusion-competent particles to undergo hemifusion becomes longer as the concentration of IgG/Fab increases.

Hemifusion times increase in a sigmoidal fashion from baseline values of 46 and 30 s at zero IgG/Fab for the H1N1 and H3N2 strains, respectively (Table S2), to two- to threefold larger plateau values at high IgG/Fab concentrations. The existence of this upper plateau is surprising; a decreasing number of available HA trimers would be expected to result in a continuous increase of hemifusion times. From the existence of the upper plateau, it would appear that HA trimers have a temporal window of opportunity following acidification to induce fusion.

To gain further insight into the fusion mechanism, we obtained hemifusion kinetics for a large number of virus particles

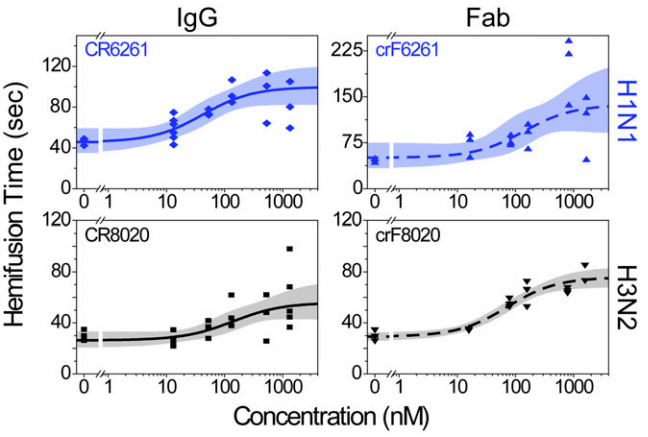

Fig. 3. Hemifusion is delayed at higher IgG/Fab concentrations. Data are displayed as in Fig. 2 and are fit with a hyperbolic function having a constant offset (*SI Materials and Methods*); each data point is the geometric mean hemifusion time from a single experimental run. Fold increases in hemifusion times between zero and the highest IgG/Fab concentrations are listed in Table 1.

and analyzed the shape of the hemifusion-time distributions by fitting them to a gamma distribution. In this manner, we obtain information about the speed of the rate-limiting step along the fusion pathway and the number of rate-limiting steps. This latter value has been shown to represent the number of HA required for fusion (15). This kinetic analysis requires at least 50 events to have the statistical power to determine the number of HA trimers involved (39) and because increasing IgG/Fab concentrations results in fewer fusing virions, not all concentrations could be analyzed (*SI Materials and Methods*). The rates extracted by this gamma distribution analysis (Fig. S8) report slower kinetics at high IgG/Fab concentrations and faster overall kinetics of H3N2, similar to data in Fig. 3. Such kinetic differences could arise from sequence variations between H1N1 and H3N2 HA, giving rise to slight differences in protein structure and conformational energetics. Analysis of the number of rate-limiting steps suggest that both virus strains require two to three HA trimers at all IgG/Fab concentrations analyzed (Fig. S8). From this observation, we conclude that IgG/Fab binding does not alter the molecular mechanism of fusion. Rather, when inhibition is not complete and hemifusion still occurs, it does so with the same requirement of two to three HA trimers regardless of the presence of IgG/Fab bound to HA on the viral surface.

Discussion

We describe an experimental method that relates the stoichiometry of antibody or Fab binding to the efficiency and kinetics of viral membrane fusion at the single virus particle level. Increased binding of broadly neutralizing, stem-binding antibodies or Fab concomitantly causes a decrease in hemifusion efficiency and a maximally two- to threefold increase in the time to hemifusion. We find hemifusion efficiency is reduced by half with ∼30–80 stem-binding IgG bound to virus particles, and that hemifusion is fully inhibited by ∼140–180 stem-binding IgG. Thus, a significant effect is elicited with quantities of IgG that are substantially lower than the ∼270–300 IgG we and others (30) estimate could sterically fit on the viral surface. Relating the number of IgG/Fab required to achieve half-maximum hemifusion inhibition to the number needed to fully inhibit hemifusion, we conclude that even the rather low fractional occupancies of ∼0.16–0.6 have a potent effect. Further, Fab also inhibit membrane fusion, albeit with higher stoichiometry.

Using radioisotope-labeled IgG, Taylor et al. found that ∼50 HC2 or HC10 monoclonal, head-binding IgG per virion could reduce infectivity in VNAs by half (31), drastically lower than their estimates of 1,000 HA trimers per H7N1 virion. In contrast, Knossow et al. (18) used comparable IgG and methodologies with the H3N2 virus to find that complete viral neutralization occurred with IgG:HA ratios of 0.2:0.33, interestingly in a similar range as the 0.38:0.47 ratios we have determined. Whereas Knossow et al. attributed neutralization solely to inhibition of cellular binding, we recently demonstrated that head-binding antibodies also prevent the release of viral progeny (29). Our single-particle fusion assay avoids the convolution of multiple outcomes from IgG binding and focuses solely on membrane fusion. Overall, our results indicate that many epitopes on HA, and likely many HA trimers, remain unbound on the surface of fusion-inhibited virions.

Our data reveal a need for two to three HA trimers for fusion and strongly support a kinetic model of HA-mediated fusion requiring simultaneous action of multiple, neighboring trimers (15, 16). This model requires only the stochastic behavior of the HA trimers in combination with a high HA surface density. It also implies the existence of a dynamic network of potential folding partners between HA on the viral surface that is established by their relative geometry and spacing, and not necessarily by physical interactions between them. Network connections become activated to mediate fusion when HA trimers stochastically unfold at low pH. If a sufficient number of HA trimers are close enough in space and are refolding within a sufficiently short window of time, then they are able to coordinate their work and mediate the onset of lipid hemifusion. Prolonged exposure to low pH induces nonproductive HA refolding (40) and serves to disrupt the HA coordination network. Timing of the fusion process, thus, represents the interplay between (*i*) low pH-induced, stochastic firing of individual HA trimers; (*ii*) stochastic coordination between refolding HA trimers to mediate membrane fusion; and (*iii*) low pH-induced inactivation of the unfolded HA (Fig. 4).

To account for the observed kinetic changes and low stoichiometries, we propose that IgG/Fab binding to block HA low-pH unfolding (23, 24, 29) inactivates network connections and lowers the probability of having a critical number of active HA trimers that are spaced closely enough to mediate fusion (Fig. 4). The elimination of neighbor–neighbor connections would then prevent the amassing of triggered HA into a density sufficient for membrane fusion to occur, even though some HA were still unbound and, likely, responsive to acidification. When a virus bound by IgG/Fab does fuse, the removal of active HA could lead to a longer elapsed time before sufficient neighboring HA trimers are able to coordinate their conformational changes. Such an interpretation is consistent with our finding that IgG/Fab binding causes slower hemifusion kinetics and with the results of a recent kinetic simulation of HA-mediated fusion (16).

In comparing the two viral strains, we find that maximum hemifusion inhibition of the H3N2 strain requires ∼3.8-fold more Fab than IgG whereas the H1N1 strain requires only ∼1.6-fold more Fab. Additionally, the H3N2 strain displays a larger fractional occupancy than does H1N1. Kinetically, the two viral strains exhibit differences in their baseline fusion rates (Fig. 3), indicative of inherent differences between them. As such, stoichiometry differences could be related to these interstrain differences, or, among other possible variations, to differences in the affinity and/or accessibility of the different epitopes on the viral surface, variations in surface protein density, or variation in virus strain composition (7, 37, 41). Additionally, it is plausible that the proximity of the CR(F)8020 epitope to the viral membrane, compared with the CR(F)6261 epitope (Fig. 1*A*), could potentially influence the binding angle of a Fab differently than

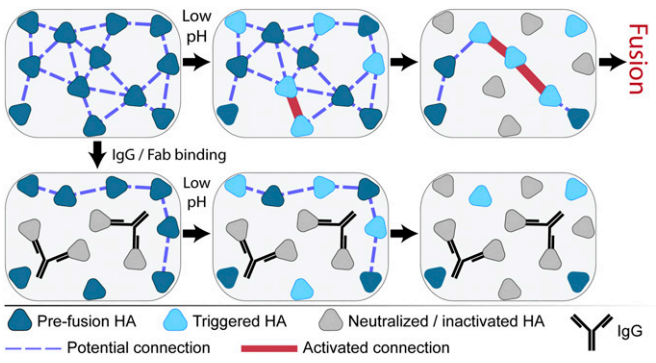

Fig. 4. Cartoon illustrating inter-HA network disruption by IgG binding leading to fusion inhibition. Fusogenic HA at neutral pH in the prefusion conformation (dark blue triangles) initially have a network of connections (blue dashed lines) dictated by their spatial geometry relative to one another. Binding of IgG (black Y) neutralizes the HA (light gray triangles) by preventing their low pH-induced conformational changes and disrupts coordination with neighboring HA. Exposure to low pH conditions triggers HA to unfold (light blue triangles) and activates the inter-HA network (thick red lines) between neighboring, triggered HA. Continued low pH exposure causes HA inactivation by nonproductive refolding (light gray triangles), also removing inter-HA connections. Although productive fusion could arise at locations with a sufficiently high density of activated inter-HA connections, both IgG/Fab binding and low pH inactivation can inhibit accumulation of this density even in the presence of fusogenic HA. NA and M2 proteins are not depicted for clarity.

an IgG. Further, large variations in the number of Fab compared with IgG may be common. Using the aforementioned HC2 and HC10, Schofield et al. (42) reported a requirement of 86- and >1,900-fold more Fab than IgG, respectively, to achieve similar levels of viral neutralization. Together, these results emphasize the enhancement in stoichiometric effectiveness that can be imparted to IgG through bivalent binding. Moreover, we find similar outcomes for both viral serotypes bound with similar numbers of IgG in terms of membrane fusion inhibition and kinetic delay.

In conclusion, we report the use of a single virus particle assay to measure the binding stoichiometry of broadly neutralizing, stem-binding antibodies and relate it solely to their functional effect of inhibiting HA-mediated membrane fusion. The data we report here sheds light both on the mechanism of inhibition by IgG/Fab and the function of HA itself during the membrane fusion process.

Materials and Methods

Proteoliposomes containing the sialoglycoprotein glycophorin A (GYPA) (full-length with GST tag; Abnova) were formed as previously described (29). Multilamellar proteoliposomes were incubated in glass-bottomed microfluidic channels to form contiguous, planar bilayers.

Influenza A virus strains A/Puerto Rico/8/34 (H1N1) and A/Aichi/68/X:31 (H3N2) were purchased from Charles River (2 mg/mL total viral protein) and used without further purification. Labeling involved virus diluted at 1:3 into Hepes buffer and mixed with octadecyl rhodamine B lipophilic dye (R18; Invitrogen, Inc.) in DMSO with a final concentration of 1 μM dye and <0.5% DMSO for 3 h. PD-10 desalting columns (GE Healthcare) removed unincorporated dye; three fractions of 200 μL with the highest particle count were pooled and used for fusion experiments.

Fusion experiments were conducted as previously described (29): 1-h virus incubation with labeled IgG/Fab, bilayer immobilization, and fluorescein-labeled streptavidin (Invitrogen) addition. An Olympus IX-71 inverted microscope was used with a 60×, TIRF (Total Internal Reflection Fluorescence) objective and 488- and 561-nm lasers (Sapphire; Coherent, Inc.). Green and red emissions were visualized on either half of an electron-multiplying CCD camera (Hamamatsu Photonics) using dual-view systems (either home-built or from Photometrics). Fusion was initiated by adding pH 5.0 citric acid buffer and fusion events recorded with 200-ms exposure at pH 5.0. Fluorescence intensity from individual IgG/Fab molecules adsorbed to clean glass in pH 5.0 buffer was acquired under identical illumination conditions.

Data analysis was performed using custom MATLAB (Mathworks, Inc.) scripts, similar to those previously described (15, 29). Briefly, viruses were identified in the red channel and paired with separately identified locations in the green channel. After correction for illumination profile and background, fluorescence trajectories were extracted and analyzed manually to select particles showing dequenching behavior. Experiments with fewer than 25 virions in a field of view were rejected. For stoichiometry calculations, green-channel trajectories were averaged for 15 frames (3 s) beginning 1 s after the pH drop (Fig. 1*D*). The number of virus-bound IgG/Fab molecules was quantified as a ratio of their integrated intensity when virus-bound to the integrated intensity of IgG/Fab individually (*SI Materials and Methods*). Time to hemifusion is the elapsed time from pH drop to the onset of hemifusion dequenching.

ACKNOWLEDGMENTS. J.J.O. thanks Dr. Marc Stuart for assistance with electron microscopy, Drs. Fabrizia Fusetti and Alicja Filipowicz-Szymanska for assistance with mass spectrometry, and the NIH and the National Institute of General Medical Sciences for a Molecular Biophysics Training Grant.

1. Han T, Marasco WA (2011) Structural basis of influenza virus neutralization. *Ann N Y Acad Sci* 1217:178–190.
2. Fleishman SJ, et al. (2011) Computational design of proteins targeting the conserved stem region of influenza hemagglutinin. *Science* 332(6031):816–821.
3. Burton DR, Poignard P, Stanfield RL, Wilson IA (2012) Broadly neutralizing antibodies present new prospects to counter highly antigenically diverse viruses. *Science* 337(6091):183–186.
4. Steel J, et al. (2010) Influenza virus vaccine based on the conserved hemagglutinin stalk domain. *MBio* 1(1), 10.1128/mBio.00018-10.
5. Vanderlinden E, et al. (2010) Novel inhibitors of influenza virus fusion: Structure-activity relationship and interaction with the viral hemagglutinin. *J Virol* 84(9): 4277–4288.
6. Klasse PJ, Sattentau QJ (2002) Occupancy and mechanism in antibody-mediated neutralization of animal viruses. *J Gen Virol* 83(Pt 9):2091–2108.
7. Klasse PJ (2008) *Desk Encyclopedia of General Virology*, eds Mahy BWJ, van Regenmortel MHV (Academic, Oxford), pp 404–410.
8. Wilson IA, Skehel JJ, Wiley DC (1981) Structure of the haemagglutinin membrane glycoprotein of influenza virus at 3 A resolution. *Nature* 289(5796):366–373.
9. Waterfield M, Scrace G, Skehel J (1981) Disulphide bonds of haemagglutinin of Asian influenza virus. *Nature* 289(5796):422–424.
10. Tong S, et al. (2013) New world bats harbor diverse influenza A viruses. *PLoS Pathog* 9(10):e1003657.
11. Bullough PA, Hughson FM, Skehel JJ, Wiley DC (1994) Structure of influenza haemagglutinin at the pH of membrane fusion. *Nature* 371(6492):37–43.
12. Harrison SC (2008) Viral membrane fusion. *Nat Struct Mol Biol* 15(7):690–698.
13. Mittal A, Bentz J (2001) Comprehensive kinetic analysis of influenza hemagglutinin-mediated membrane fusion: Role of sialate binding. *Biophys J* 81(3):1521–1535.
14. Danieli T, Pelletier SL, Henis YI, White JM (1996) Membrane fusion mediated by the influenza virus hemagglutinin requires the concerted action of at least three hemagglutinin trimers. *J Cell Biol* 133(3):559–569.
15. Floyd DL, Ragains JR, Skehel JJ, Harrison SC, van Oijen AM (2008) Single-particle kinetics of influenza virus membrane fusion. *Proc Natl Acad Sci USA* 105(40): 15382–15387.
16. Ivanovic T, Choi JL, Whelan SP, van Oijen AM, Harrison SC (2013) Influenza-virus membrane fusion by cooperative fold-back of stochastically induced hemagglutinin intermediates. *ELife Sciences* 2:e00333.
17. Bizebard T, et al. (1995) Structure of influenza virus haemagglutinin complexed with a neutralizing antibody. *Nature* 376(6535):92–94.
18. Knossow M, et al. (2002) Mechanism of neutralization of influenza virus infectivity by antibodies. *Virology* 302(2):294–298.
19. Dreyfus C, et al. (2012) Highly conserved protective epitopes on influenza B viruses. *Science* 337(6100):1343–1348.
20. Ekiert DC, et al. (2012) Cross-neutralization of influenza A viruses mediated by a single antibody loop. *Nature* 489(7417):526–532.
21. Lee PS, et al. (2012) Heterosubtypic antibody recognition of the influenza virus hemagglutinin receptor binding site enhanced by avidity. *Proc Natl Acad Sci USA* 109(42):17040–17045.
22. Throsby M, et al. (2008) Heterosubtypic neutralizing monoclonal antibodies cross-protective against H5N1 and H1N1 recovered from human IgM+ memory B cells. *PLoS ONE* 3(12):e3942.
23. Ekiert DC, et al. (2009) Antibody recognition of a highly conserved influenza virus epitope. *Science* 324(5924):246–251.
24. Ekiert DC, et al. (2011) A highly conserved neutralizing epitope on group 2 influenza A viruses. *Science* 333(6044):843–850.
25. Sui J, et al. (2009) Structural and functional bases for broad-spectrum neutralization of avian and human influenza A viruses. *Nat Struct Mol Biol* 16(3):265–273.
26. Okuno Y, Isegawa Y, Sasao F, Ueda S (1993) A common neutralizing epitope conserved between the hemagglutinins of influenza A virus H1 and H2 strains. *J Virol* 67(5):2552–2558.
27. Corti D, et al. (2011) A neutralizing antibody selected from plasma cells that binds to group 1 and group 2 influenza A hemagglutinins. *Science* 333(6044):850–856.
28. Nakamura G, et al. (2013) An in vivo human-plasmablast enrichment technique allows rapid identification of therapeutic influenza A antibodies. *Cell Host Microbe* 14(1): 93–103.
29. Brandenburg B, et al. (2013) Mechanisms of hemagglutinin targeted influenza virus neutralization. *PLoS ONE* 8(12):e80034.
30. Harris AK, et al. (2013) Structure and accessibility of HA trimers on intact 2009 H1N1 pandemic influenza virus to stem region-specific neutralizing antibodies. *Proc Natl Acad Sci USA* 110(12):4592–4597.
31. Taylor HP, Armstrong SJ, Dimmock NJ (1987) Quantitative relationships between an influenza virus and neutralizing antibody. *Virology* 159(2):288–298.
32. Parren PW, Burton DR (2001) The antiviral activity of antibodies in vitro and in vivo. *Adv Immunol* 77:195–262.
33. Reading SA, Dimmock NJ (2007) Neutralization of animal virus infectivity by antibody. *Arch Virol* 152(6):1047–1059.
34. Otterstrom J, van Oijen AM (2013) Visualization of membrane fusion, one particle at a time. *Biochemistry* 52(10):1654–1668.
35. Tiffany JM, Blough HA (1970) Models of structure of the envelope of influenza virus. *Proc Natl Acad Sci USA* 65(4):1105–1112.
36. Inglis SC, Carroll AR, Lamb RA, Mahy BW (1976) Polypeptides specified by the influenza virus genome I. Evidence for eight distinct gene products specified by fowl plague virus. *Virology* 74(2):489–503.
37. Moulès V, et al. (2011) Importance of viral genomic composition in modulating glycoprotein content on the surface of influenza virus particles. *Virology* 414(1):51–62.
38. Harris A, et al. (2006) Influenza virus pleiomorphy characterized by cryoelectron tomography. *Proc Natl Acad Sci USA* 103(50):19123–19127.
39. Floyd DL, Harrison SC, van Oijen AM (2010) Analysis of kinetic intermediates in single-particle dwell-time distributions. *Biophys J* 99(2):360–366.
40. Weber T, et al. (1994) Evidence for H(+)-induced insertion of influenza hemagglutinin HA2 N-terminal segment into viral membrane. *J Biol Chem* 269(28):18353–18358.
41. Shaw ML, Stone KL, Colangelo CM, Gulcicek EE, Palese P (2008) Cellular proteins in influenza virus particles. *PLoS Pathog* 4(6):e1000085.
42. Schofield DJ, Stephenson JR, Dimmock NJ (1997) Variations in the neutralizing and haemagglutination-inhibiting activities of five influenza A virus-specific IgGs and their antibody fragments. *J Gen Virol* 78(Pt 10):2431–2439.

Supporting Information

Otterstrom et al. 10.1073/pnas.1411755111

SI Materials and Methods

Microfluidic Flow Cell and Glass Cleaning. Experiments were performed in microfluidic channels formed using either double-sided tape sandwiched between a quartz top and coverslip bottom as described previously (1), or multichannel polydimethylsiloxane (PDMS) chips. PDMS (Slygard 184; Dow Corning)-based multichannel microfluidic chips were formed by standard PDMS cast-molding techniques (2, 3). Each chip housed five microfluidic channels having inner dimensions 0.5 (width) × 0.2 (height) × 10 (length) mm^3 and separated by 0.5 mm. PDMS chips were nonpermanently adhered to the surface of the cleaned glass microscope coverslips (no. 1 thickness; VWR) and housed in a home-built microscope adapter. Inlet and outlet polyethylene tubing (PE20 and PE60, respectively; Intramedic) was coupled to each microfluidic channel to allow for rapid buffer exchange via connection to a syringe pump (NE-1000; New Era Pump Systems, Inc.). All chips and flow channels were used only once.

Virus and IgG/Fab Labeling. Influenza A strains PR/8/34 (H1N1) and A/Aichi/2/68 (X-31, H3N2) propagated in specific pathogen-free eggs were purchased from Charles River and used without further purification. Stock samples were certified by the manufacturer to have 2 mg total viral protein per milliliter. EM confirmed that the viruses used were monodisperse, spherical particles of uniform size (Fig. S6), the latter being due to the method of virus propagation. Labeling was performed by diluting virus stocks 1:3 into HNE buffer (5.0 mM Hepes, 140 mM NaCl, 0.2 mM EDTA, pH 7.4), then adding a 0.5% volume equivalent of octadecyl rhodamine B lipophilic dye (R18; Invitrogen, Inc.) in DMSO to a final dye concentration of 1 μM. The virus–dye mixture was placed on a rotating microtube mixer (Cole-Parmer) for 3 h. Unincorporated dye was removed using a PD-10 desalting column (GE Healthcare), causing ∼10-fold virus dilution. Fractions of 200 μL were collected and checked for labeled virus using the microscope setup. The three to four fractions with the highest particle count were pooled into a single volume, aliquoted, frozen using liquid nitrogen, and stored at −80 °C until use. Labeled viruses were confirmed to be infectious (4).

IgG and Fab Production. Human IgG1 antibodies CR6261 and CR8020, were constructed by cloning the heavy and light chain variable regions into a single expression vector containing the IgG1 constant regions. HEK293-F cells were transfected with the IgG expression constructs and the expressed antibodies were purified from serum-free culture supernatants using protein A chromatography (HiTrap; GE Healthcare) followed by a desalting step (HiPrep 26/10; GE Healthcare). The Fab fragments were obtained by IdeS digestion of the purified IgG, followed by protein G purification (GE Healthcare), cation exchange (MonoS; GE Healthcare), and gel filtration (Superdex200; GE Healthcare).

IgG/Fab Labeling and Degree of Labeling Determination. HA-specific antibodies CR6261 and CR8020 were fluorescently labeled with Alexa Fluor 488 (AF488; Molecular Probes) according to manufacturers' guidance. In brief, IgG/Fab fragments were added to AF488 dye in sodium bicarbonate buffer. The solutions were mixed at moderate speed on a Ferris wheel mixer for 2 h and protected from light. Free dye was removed from the sample using a PD10 desalting column (GE Healthcare). AF488-labeled IgG/Fab were eluted into 20 mM sodium acetate, 75 mM NaCl, 5% (vol/vol) sucrose, pH 5.5.

The number of AF488 molecules bound to the IgG/Fab molecules was determined using photobleaching analysis and MALDI mass spectrometry. The degree of labeling was taken as an average of these two results and the percentage of labeled IgG/Fab molecules visualized was estimated from a Poisson calculation (Table S1).

Photobleaching measurements were performed by adsorbing labeled IgG/Fab molecules to a clean glass surface and illuminating with ∼5 W/cm^2 488-nm laser power to observe individual photobleaching steps. Distributions of the final bleaching height were extracted and well fit by Gaussian distributions. The initial fluorescence intensity of visualized molecules was divided by the mean intensity identified by Gaussian fitting to obtain the distributions for the number of fluorophores bound to each IgG/Fab (Fig. S3 *A*, *i* and *B*, *i*). These distributions for IgG were well fit by Poisson distributions to determine the expected number of covalently linked Alexa-488 molecules. The distributions for Fab were reasonably well fit by Poisson distributions, but showed higher than expected population densities at a lower number of linked Alexa-488 molecules, indicating that not all available N-terminal amino groups are equally accessible for labeling.

MALDI mass spectra at mass-to-charge ratios of one ($m/z = 1$) and two ($m/z = 2$) were obtained for unlabeled and Alexa-488–labeled IgG/Fab using sinapinic acid as the matrix. The peak value in the mass spectra of the unlabeled IgG/Fab was subtracted from the mass spectra of the labeled molecules. The shifted mass spectra of the labeled molecules was then divided by the mass of individual Alexa-488 molecules, determined to be 515 Da using molecular structures provided by the manufacturer, to scale the mass values in terms of numbers of covalently linked Alexa-488 molecules (Fig. S3). The resulting spectra were well fit by Poisson distributions to identify the expected number of Alexa-488 per IgG/Fab (Fig. S3 *A*, *ii* and *B*, *ii*).

Proteoliposome Preparation. Proteoliposomes were composed of a $0.8{:}0.2{:}2.5{\times}10^{-5}$ ratio of molar fractions of DOPC:CH:biotin-DHPE [respectively 1,2-dioleoyl-sn-glycero-3-phosphocholine and Cholesterol (Avanti Polar Lipids); *N*-((6-(biotinoyl)amino) hexanoyl)-1,2-dihexadecanoyl-sn-glycero-3-phosphoethanolamine triethylammonium salt (Invitrogen)] mixed in chloroform solutions, dried under argon, and then desiccated for 2 h. Dried lipids were suspended in HNE buffer at 5 mg/mL, freeze–thawed five times, then extruded using 0.2 μm-pore size polycarbonate filters (miniextruder; Avanti). Liposomes were solubilized by Triton X-100 (molecular biology grade; VWR International) to a final concentration of 0.5% and incubated at 37 °C for 15 min, then on ice for 15 min. The GYPA (Abnova; full-length recombinant protein with a GST tag) was added to solubilized lipids at a lipid:protein molar ratio of ∼1:40,000 and mixed at 4 °C for 30 min. Bio-Beads (SM-2 absorbent; Bio-Rad Laboratories, Inc.) removed the Triton-X detergent through two subsequent 2-h incubations at 4 °C with constant rocking, using 200 mg Bio-Beads per 300 μL solution. Proteoliposome preparations were stored at 4 °C under an argon atmosphere for up to 48 h before use with no further treatment.

Glycophorin A membrane protein was used in lieu of membrane-bound gangliosides, such as GD1a (1) because we found that the H1N1 virus strain did not become immobilized upon planar bilayers when sialic acid was presented in this fashion, including use of ganglioside mixtures (catalog no. 345717;

Calbiochem) and S-Sialyl-a(2,6)-lactosylceramide (Wako Pure Chemical Industries). Both the H1N1 and H3N2 virus strains used bound to planar bilayers comprising the GYPA membrane protein, although the numbers of immobilized viruses exhibited a substantial amount of fluctuation between experimental runs (Fig. S2). The requirement by H1N1 to use GYPA rather than a ganglioside for immobilization also reduced the degree of control over the amount of sialic acid receptor on the bilayer surface because each GYPA protein contains multiple sialic acid moieties.

Microscope Specifications. Measurements were conducted on an inverted fluorescence microscope (Olympus IX-71) equipped with a custom-ordered microscope filter cube (filters zet488/561m and zt488/561rpc; Chroma Ltd.) and either a 60× N.A. 1.49 objective (Olympus APON60OTIRF) or a 60× N.A. 1.45 objective (PLANAPON60TIRF; Olympus). The N.A. 1.45 objective was found to exhibit less chromatic aberration at the edge of the images, improving the colocalization between the virus and IgG/Fab signal. Virus particles and labeled IgG/Fab were illuminated, respectively, with ∼0.25 W/cm^2 561-nm and ∼0.2 W/cm^2 488-nm continuous-wave solid state lasers (Sapphire models; Coherent, Inc.) focused onto the back-focal plane of the microscope objective and aligned in objective-based TIR mode. The configuration was optimized to homogeneously illuminate the entire virus particle and the fluorescence intensity of labeled IgG/Fab bound to viruses was found to be independent at TIR incidence angles less than 57° (Fig. S5), while still suppressing background fluorescence. Emitted green and red fluorescence was separated by a home-built dual-view system with a Thorlabs DMLP567 long-pass filter or by a commercial Dual-View system (Photometrics) with a Chroma T560LPXR long-pass filter. Signals were filtered to remove stray laser light and background from Raman scattering (Chroma ET525-50m and ET605-70m, green and red respectively), then focused onto either half of an electron-multiplying CCD camera (Image-EM model C9100-13; Hamamatsu Photonics K.K.). False-color representative images resulting from this setup are depicted in Fig. 1.

Fusion Experiment. Glass-supported planar bilayers were formed by adding the proteoliposome solution to a HNE-hydrated microfluidic flow cell mounted on the microscope and incubated with the glass surface for a minimum of 45 min at room temperature. R18-labeled viruses were diluted 10-fold into a solution of 100% Alexa-488–labeled IgG/Fab, bringing the IgG/Fab to the desired final concentration. We estimate a virus particle concentration of $\sim 6 \times 10^{12}$ per milliliter during IgG/Fab incubation, calculated using previous measurements that 37% of the total virus protein is HA (5) and that there are 375 HA trimers per virus (6, 7). This concentration was found to be the most dilute concentration of virus that allowed for sufficient virion immobilization on the bilayer surface while gathering reasonable statistics. Virus and IgG/Fab were incubated for 45–60 min at room temperature, and then added to the microfluidic flow cell at 5 μL/min, wherein the viruses immobilized on the planar bilayer through specific HA–GYPA interactions. Fluorescein-labeled streptavidin (Invitrogen) was subsequently added at 0.2 μg/mL using a flow rate of 10 μL/min for 5 min; therein the labeled IgG/Fab not bound to viruses washed away to leave a low background. A 2-min wash with clean HNE buffer at a high (100 μL/min) rate removed unbound viruses, IgG, and streptavidin-fluorescein. Finally, viral fusion was initiated by rapid injection of a citric acid buffer (10.0 mM citric acid, 140 mM NaCl, 0.2 mM EDTA, pH 5.0) at 200 μL/min and recorded using Metavue imaging software (Life Science Imaging Ltd.) at an acquisition rate of 5 Hz for 240 s and maximal EM gain. Laser illumination during the first 5–6 s and before the pH drop was with 561 nm only, then the 488-nm illumination was initiated. This alternation allowed for identification of viruses in the red channel, then colocalization in the green channel. Total laser illumination was ∼400 mW/cm^2 and was set such that at high neutralizing molecule concentration there were very few saturated pixels together with a large range of pixel intensity values. Following immobilization of the virus on the bilayer surface, the fusion experiments required 10–20 min total experimental time.

Data Extraction and Analysis. The laser illumination profile in each channel was identified after the pH drop by smearing out fluorescent peaks with a 40-pixel radius median filter, which allowed for the fitting of the underlying beam profile with a 2D Gaussian. The fitted profile was set to have a maximal value of one at its peak. Each image extracted from the recording was corrected for the illumination profile (flattened) by first removing dark counts and then dividing by the fitted profile.

Individual viral particles were identified and their fluorescent trajectories extracted using a custom MATLAB code similar to that described previously (1). The arrival of the low-pH buffer was detected, as previously described (1), as a sudden loss of fluorescein signal in the green channel. Red-channel fluorescence peaks were identified by averaging 10 frames under 561-nm illumination only, flattening and removing global fluorescence background (see below), and then applying a discoidal averaging filter (8). Peaks were identified by thresholding using a $\mu + 2 \times \sigma$ criterion, where μ and σ are the average intensity and intensity SD, respectively, of the filtered red channel. Green-channel peaks were similarly identified by averaging 10 frames after the pH drop. Colocalization was achieved by translating the locations found in the red channel onto the green channel and grouping the nearest-neighbor pairs of peaks.

Peaks in the green channel were fit with a 2D Gaussian profile and all pixels within 3σ of the peak center were identified for signal integration; red-channel peaks were surrounded with a 4 × 4-pixel square box for fluorescence signal integration. Fluorescence background in the green channel was identified on a per-particle basis as the baseline offset resulting from Gaussian fitting, whereas the red-channel background was found globally by taking the peak of the distribution of the pixel intensities from the flattened image used for particle colocalization.

Red-channel fluorescent trajectories were plotted and manually selected as exhibiting hemifusion similar to previous description (1). Those showing clear dequenching spikes followed by dissipative signal loss, as shown in the Fig. 1*B*, were directly classified as fusing virions. Trajectories showing characteristics of dequenching and/or dissipative signal loss, but that were not as overtly similar to the trajectory of Fig. 1*B*, were subjected to further manual inspection. In these cases, a virus particle in question is observed in the recorded fusion movie and those showing a rapid, outward movement of R18 molecules away from the virus identifiable by eye were also classified as fusing virions. Absolute hemifusion efficiency in each experiment was calculated as the number of particles in a field of view determined to undergo hemifusion divided by the total number of particles initially detected in the same field of view. Hemifusion efficiency data were fit using a four-parameter logistic model using the transform-both-sides approach for variance stabilization (9) using a logit transformation (Table S2, Eq. **S1**). For fitting, conditions with no fusion events were set to one event.

The integrated green-channel fluorescence corresponding to the virus-bound-labeled IgG/Fab was averaged over 15 frames (3 s), starting five frames (1 s) after the pH drop (dark green square in Fig. 1*C*). Separately, the average integrated intensity of individual labeled IgG or Fab molecules was obtained by nonspecifically adsorbing them to a clean glass surface within a microfluidic channel and measuring their fluorescence intensity under identical illumination conditions as used in the fusion experiments (Fig. S5). Laser power was varied to ensure fluorophore

excitation occurred within the linear response regime (Fig. S5) and to obtain photobleaching data (Fig. S3).

The number of molecules bound to HA on the surface of each virus was calculated by dividing the average integrated fluorescence intensity measured from the fusion experiments by the average integrated intensity measured for individual IgG/Fab molecules. When determining the intensity corresponding to individual IgG/Fab molecules, the illumination conditions were such that fluorescence intensity was independent of the TIRF angle and was linearly dependent upon the incident laser power density (Fig. S5). In standard TIRF microscopy, the illumination beam has penetration depths near 200 nm into the sample. We chose a TIRF angle of 57° that was far from the critical angle of 61° required for TIR. As a result, excitation light propagated through the sample at a highly inclined angle, rather than undergoing reflection. This illumination design is similar to highly inclined and laminated optical sheet microscopy (10). Therein, Tokunaga et al. imaged samples at depths of 15 μm with only 40% loss of fluorescence intensity, whereas we imaged our ∼120-nm viruses at penetration depths ∼100-fold lower. Our shallow imaging depth combined with our illumination angle far from the critical angle would suggest that the rapidly decaying penetration depth relevant to standard TIRF microscopy is not likely to significantly affect our measurements.

The value for the number of IgG/Fab bound to each virus was corrected for the presence of unlabeled IgG/Fab using the visualized fraction measured by MALDI and photobleaching (Table S1). To this end, the number of IgG/Fab calculated to be bound to each virion was multiplied by a correction factor corresponding to one divided by the visualized fraction. We have used the correction factor found using the average number of dyes per IgG/Fab molecule. Using only the result from photobleaching measurements would result in 0.7–6.9% additional IgG/Fab bound to the viruses (2.8% average), whereas using only the MALDI result would result in 0.3–3.2% fewer IgG/Fab bound to the viruses (1.4% average). For each experimental run, the distribution for the numbers IgG/Fab bound to all virions (both fusing and nonfusing) was corrected for unlabeled IgG/Fab and its median value calculated (Fig. 2). The median values for the numbers of IgG/Fab bound were fit with a hyperbola using the transform-both-sides approach for variance stabilization (9) using a square-root transformation (Table S2, Eq. **S2**).

Numbers of IgG/Fab were related to hemifusion efficiency by the following: For a given number of bound IgG or Fab, the corresponding IgG/Fab concentration was estimated and used to estimate the corresponding hemifusion efficiency with 95% confidence interval (error propagation using proc NLMIXED Version 9.2; SAS), using the delta method (11, 12) and the lowest degrees of freedom from the two models.

Hemifusion time to event for each particle was determined as the elapsed time between the pH-drop frame and the frame when hemifusion occurs, defined as the time point with the maximal rate of fluorescence increase. The time-to-hemifusion distribution for each experimental run was determined and its geometric mean time and geometric SD (error) determined. The geometric mean was used to preserve the semilog distribution, often used to analyze waiting time distributions (13). The times resulting from each experiment were $\log_{10}$ transformed and fitted by a hyperbola with a constant offset (Table S2, Eq. **S3**). The geometric means in the absence of IgG/Fab reported in *Results* (46 s for H1N1; 30 s for H3N2) are comparable to estimates obtained from data fitting (Table S2), indicating our models were properly anchored.

Distributions of hemifusion times that we have obtained previously (1) and in the current work (Fig. S8) show a rise and decay in the frequency of events. As described in Floyd et al. (1) such an observation indicates that hemifusion does not occur through a single, one-step biochemical transition, rather that intermediate states exist in the biochemical process leading to hemifusion. In the previous work of Floyd et al. (1), we used the gamma distribution to obtain estimates for the rate of the rate-limiting step in the hemifusion process, k, and the number of independent steps that must be present for hemifusion to occur, N:

$$P(t|k,N) = \frac{k^N t^{N-1}}{\Gamma(N)} \exp(-kt).$$

Floyd et al. reported that $N > 1$ and that this trend was independent of proton concentration, which triggers the HA to unfold and mediate fusion. Such an observation is consistent with N independent steps acting in parallel, each with rate k, and, therefore, that the N parameter corresponds to the number of HA trimers reacting to low pH (high proton concentration) to mediate hemifusion.

Fit parameters for the gamma distribution found for hemifusion times measured here in the presence of IgG/Fab are presented in Fig. S8. There, the N parameter does not drop below 1, staying in the range of 2 to 3 as observed previously (1). We therefore conclude that $N > 1$ at both limiting proton concentrations (1) and following removal of fusogenic HA trimers (Fig. S8). As discussed in the main text, only experimental runs where 50 or more hemifusion times were obtained were used for analysis by fitting with this distribution, in accord with supplemental reference (14). Fit parameters were calculated, equivalently, using fitting standard algorithms in SAS statistical software or in MATLAB (gamfit function).

Monte Carlo Simulation. To simulate protein packing on the viral surface we used a simple 2D model. Model viral surfaces were generated using a Monte Carlo algorithm minimizing protein overlap and maximizing IgG/Fab–HA interactions. Each protein was approximated with a number of spheres (Fig. S7) such that their final dimensions were in agreement with appropriate crystal structures. Model viral membranes were composed of the envelope-embedded proteins HA, neuraminidase (NA), and M2 proton channel. Binding geometry of IgG/Fab to the HA proteins was constrained to be in agreement with the CR8020-HA cocrystal structure [PDB ID code 3SDY (15)].

IgG molecules (14 nm in total length) containing two paratopes were modeled with the Fc domain pointing vertically from the in silico viral surface and were allowed to have flexibility around their midpoint. They were constructed from five spheres: two for each fab, one representing the variable and the other the constant region, and one sphere corresponding to the Fc tail. Fab fragments (7 nm in length) were not flexible, had a single paratope, and were constructed from two spheres. HA was approximated with four spheres: one larger for the stem and three for the HA1 heads. The diameter of the HA stem was measured around the epitope area of the CR8020 antibody to assure correct binding geometry. The approximate size of the extracellular domain of the M2 proton channel was estimated from its the molecular mass, accounting for the protein's tetrameric quaternary structure. NA was modeled as a single sphere. The spike protein (HA and NA) density was set at 8,000 spikes per square micron and an HA:NA ratio of 7:1 in agreement with previous studies of similar influenza virus samples (6, 7). From this density, a surface representing our average 125-nm virus particles contained 392 spike proteins, 341 of which were HA.

Simulations were performed by placing viral proteins randomly within a 2D periodic simulation surface. The surfaces were minimized with a Monte Carlo-like algorithm to remove protein overlap from a randomly generated surface. The overlap energy was modeled as a square-well potential with an additional term proportional to the overlap surface. Increasing IgG/Fab concentrations were added and their final structure and position

determined using the Monte Carlo sampling. The paratope–epitope interaction energy was modeled using the patchy-spheres approach (16) so as to impose appropriate distances and angles between the epitope and paratope as dictated by their cocrystal structure (15). We found that using a smooth potential instead of a square-well interaction energy allowed Monte Carlo minimization to converge faster due to the longer range of protein–protein interactions. For the minimization we used the following moves: single protein rotation and perturbation, two proteins swapping, IgG/Fab jumping to another binding site, and randomizing Fab–Fab angle of the IgG. The IgG/Fab concentration at which protein overlap could not be prevented was taken as the steric packing limit.

We then used the viral surfaces to calculate the number of available binding sites parameter. This calculation was done by placing a sample IgG/Fab at every HA epitope, checking if the molecule could be placed without overlap, and summing the number of epitopes permitting the additional IgG/Fab. Also for the antibody, multiple Fab–Fab angles were tested. The number of available binding sites calculated in this manner was then averaged over the whole set of surfaces as a function of ligands already bound to the virus (Fig. S7).

Previous studies have argued that groups of HA in close proximity could represent fusogenic clusters that cause nucleation of membrane fusion events (17). Simulation data were analyzed to identify HA clusters defined to be groups of HA trimers free from IgG/Fab that were in close proximity to each other without any additional surface proteins between them; cluster disruption was defined to occur when these conditions were not met. Unfortunately defining clusters of fixed sizes from three to six neighboring HA trimers did not result in replication of trends observed in the experimental data of hemifusion efficiency, namely a need for more Fab than IgG to achieve equal cluster disruption, and the results of these analyses are not included.

1. Floyd DL, Ragains JR, Skehel JJ, Harrison SC, van Oijen AM (2008) Single-particle kinetics of influenza virus membrane fusion. *Proc Natl Acad Sci USA* 105(40): 15382–15387.
2. Delamarche E, Bernard A, Schmid H, Michel B, Biebuyck H (1997) Patterned delivery of immunoglobulins to surfaces using microfluidic networks. *Science* 276(5313):779–781.
3. Xia Y, Whitesides G (1998) Soft lithography. *Annu Rev Mater Sci* 28:153–184.
4. Brandenburg B, et al. (2013) Mechanisms of hemagglutinin targeted influenza virus neutralization. *PLoS ONE* 8(12):e80034.
5. Tiffany JM, Blough HA (1970) Models of structure of the envelope of influenza virus. *Proc Natl Acad Sci USA* 65(4):1105–1112.
6. Harris A, et al. (2006) Influenza virus pleiomorphy characterized by cryoelectron tomography. *Proc Natl Acad Sci USA* 103(50):19123–19127.
7. Harris AK, et al. (2013) Structure and accessibility of HA trimers on intact 2009 H1N1 pandemic influenza virus to stem region-specific neutralizing antibodies. *Proc Natl Acad Sci USA* 110(12):4592–4597.
8. Hedde PN, Fuchs J, Oswald F, Wiedenmann J, Nienhaus GU (2009) Online image analysis software for photoactivation localization microscopy. *Nat Methods* 6(10): 689–690.
9. Findlay JW, Dillard RF (2007) Appropriate calibration curve fitting in ligand binding assays. *AAPS J* 9(2):E260–E267.
10. Tokunaga M, Imamoto N, Sakata-Sogawa K (2008) Highly inclined thin illumination enables clear single-molecule imaging in cells. *Nat Methods* 5(2):159–161.
11. Billingsley P (1986) *Probability and Measure* (John Wiley & Sons, Inc., New York).
12. Cox C (1998) *Encyclopedia of Biostatistics*, eds Armitage P, Colton T (John Wiley, New York), pp 1125–1127.
13. Limpert E, Stahel W, Abbt M (2001) Log-normal distributions across the sciences: Keys and clues. *Bioscience* 51(5):341–352.
14. Floyd DL, Harrison SC, van Oijen AM (2010) Analysis of kinetic intermediates in single-particle dwell-time distributions. *Biophys J* 99(2):360–366.
15. Ekiert DC, et al. (2011) A highly conserved neutralizing epitope on group 2 influenza A viruses. *Science* 333(6044):843–850.
16. Huisman BA, Bolhuis PG, Fasolino A (2008) Phase transition to bundles of flexible supramolecular polymers. *Phys Rev Lett* 100(18):188301.
17. Bentz J (2000) Minimal aggregate size and minimal fusion unit for the first fusion pore of influenza hemagglutinin-mediated membrane fusion. *Biophys J* 78(1):227–245.

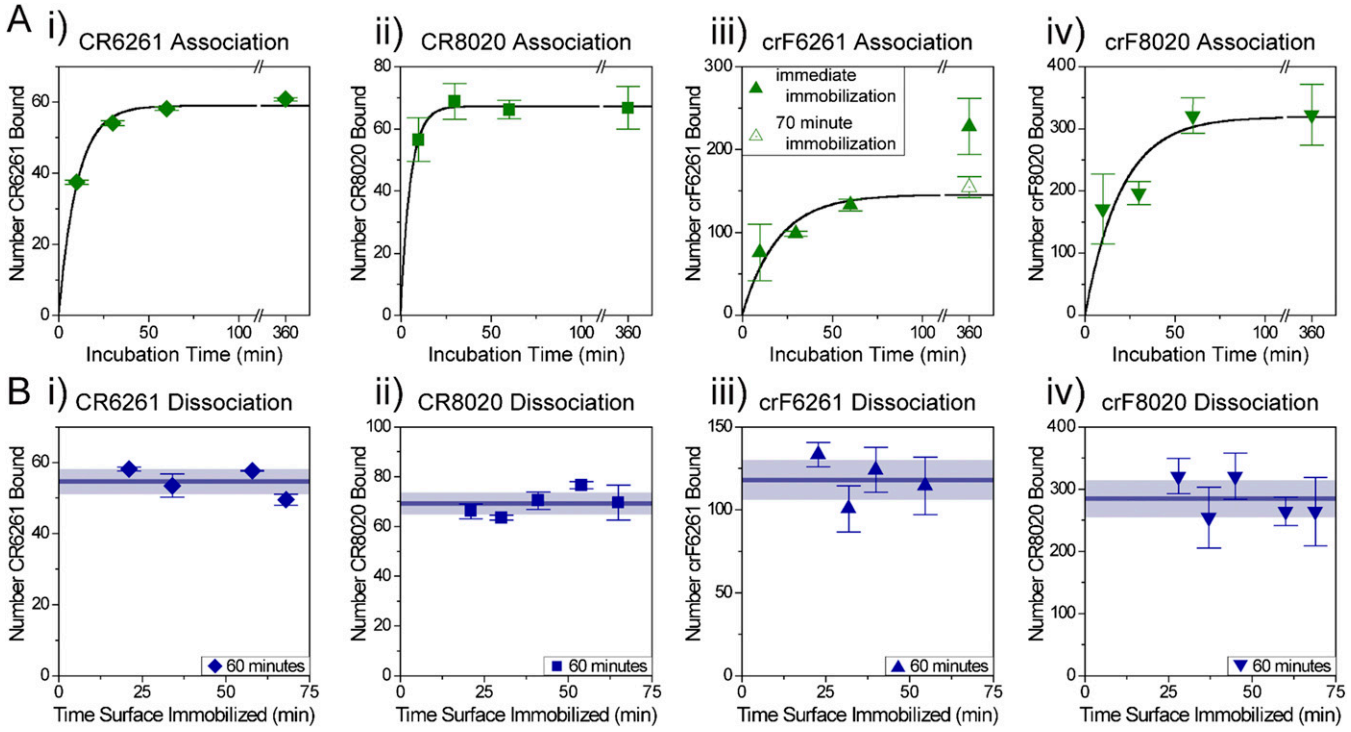

Fig. S1. Association (*A*) and dissociation (*B*) of CR6261 (*i*) and CR8020 IgG (*ii*), and of crF6261 (*iii*) and crF8020 Fab (*iv*). For IgG/Fab association plots, H1N1 (*A*, *i* and *iii*) or H3N2 (*A*, *ii* and *iv*) viruses were incubated with 130 nM IgG or Fab for the time indicated on the horizontal axis, then added to flow channels to become immobilized on the supported lipid bilayer (SLB). Flow-in time of the virus plus IgG/Fab solution was ~20 min. Two fields of view were imaged in rapid succession and the average IgG/Fab coverage ± SEM is reported. (*B*) For dissociation after immobilization, IgG/Fab coverage on the same virus samples as in *A* were quantified at ~10 to 20-min intervals without repeated imaging of the same fields of view. Fusion experiments described in the main text typically had a run time of 10 min after flow-in of the virus-IgG/Fab solution. For clarity, only dissociation measurements corresponding to 60 min incubation (blue) from *A* are shown. Mean values of the number of bound IgG/Fab ± SD over the times after immobilization are indicated by the horizontal line and shaded regions, respectively. Fluorescence intensity fluctuated between fields of view, as indicated in the scatter of the data points, but did not systematically decrease as would be expected if nonspecific binding occurred or if the IgG/Fab otherwise dissociated from the virus. Nonspecific binding occurred only for 360 min incubation of crF6261 with H1N1 (filled symbol at 360 min in *A*, *iii*), which was observed to systematically decrease to coverage levels equivalent to 60-min incubation (open-faced symbol at 360 min in *A*, *iii*) after 70 min of immobilization on the SLB surface.

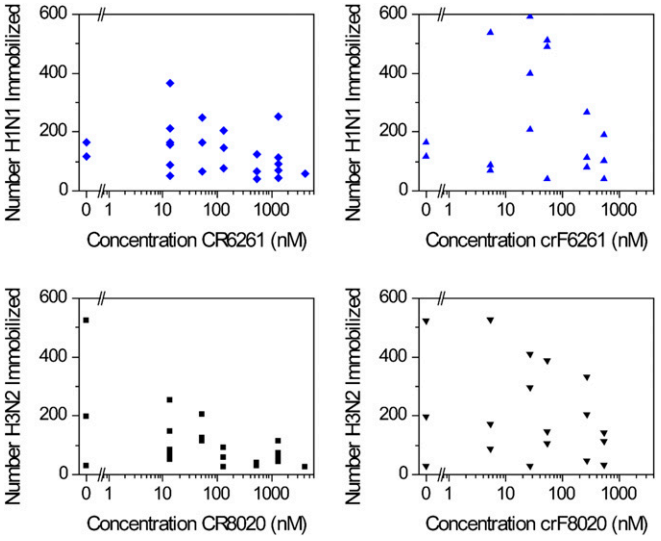

Fig. S2. Immobilization of the virus to target bilayers through glycophorin A binding was largely unaffected by IgG/Fab binding to the viral surface. Each data point corresponds to a single fusion experiment and represents the total number of virions imaged in equal-sized fields of view. Although there is some decrease in binding at the highest concentrations, many virions are still visualized, indicating that IgG/Fab binding does not prevent HA-receptor recognition.

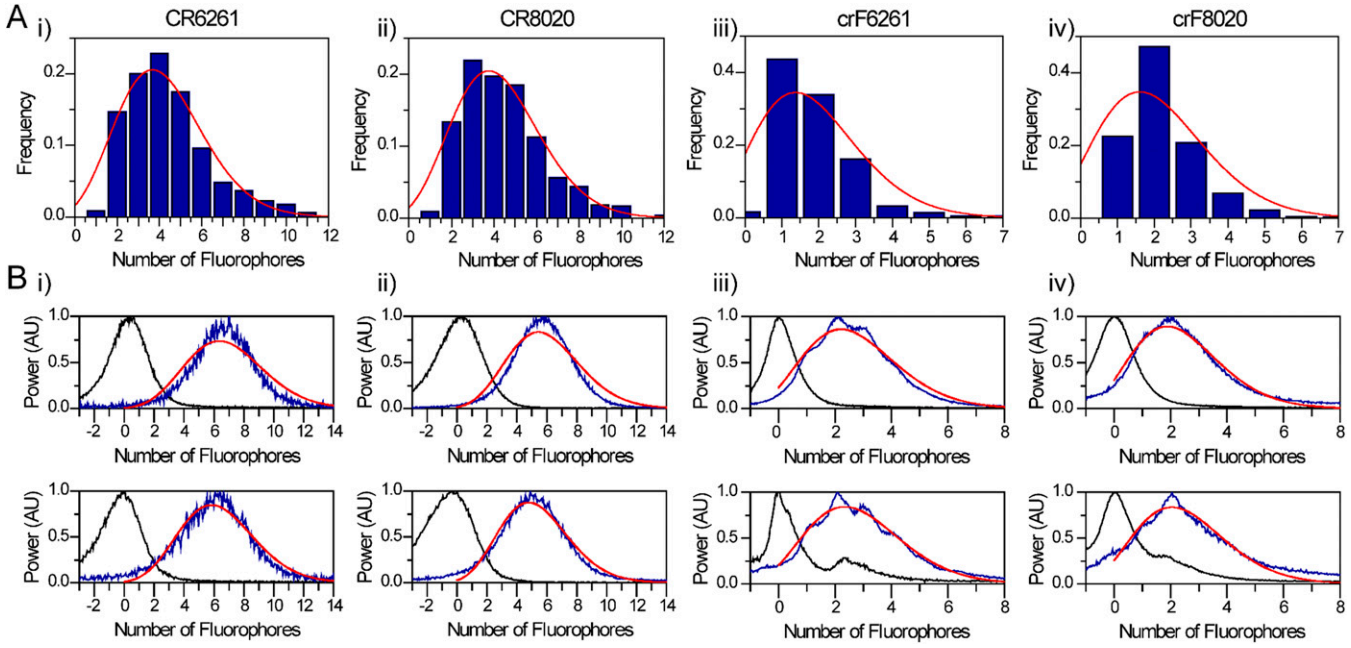

Fig. S3. Degree of Alexa-488 labeling for 6261 IgG (*i*) and Fab (*ii*), and for 8020 IgG (*iii*) and Fab (*iv*), as measured by photobleaching analysis (*A*) and MALDI mass spectrometry (*B*). (*A*) Photobleaching measurements resolved the distribution of number of Alexa-488 molecules bound to each molecule as described in *SI Materials and Methods*. These distributions were fit with a Poisson distribution (red lines) to identify the expected number of fluorophores bound to each IgG/Fab. (*B*) Mass spectra at mass:charge ratios of 1 (*Top*) and 2 (*Bottom*) were determined for the unlabeled IgG/Fab (black) and for the Alexa-488–labeled IgG/Fab (blue). The peak value from the unlabeled spectra was subtracted from each labeled spectra, and then each spectra was divided by the molecular mass of Alexa-488. The mass spectra of the labeled molecules were fit with a Poisson distribution (red) to identify the expected number of fluorophores covalently linked to each IgG/Fab. Spectra for Fab molecules resolved identifiable peaks corresponding to molecules having one, two, three, and four dye molecules (*B*, *iii* and *iv*). Results of fitting are summarized in Table S1.

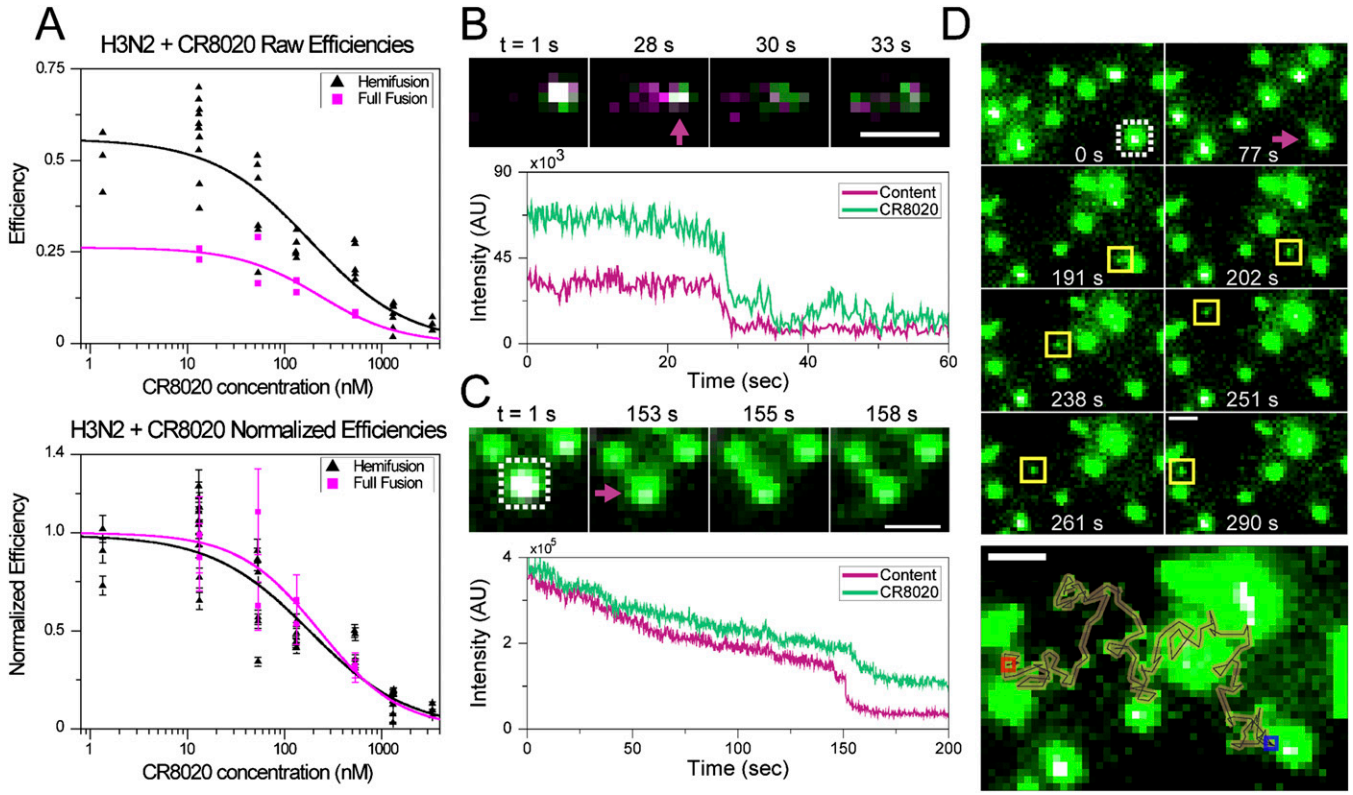

Fig. S4. CR8020 binding inhibits full fusion as well as it does hemifusion. The luminal contents of H3N2 viruses were labeled with aqueous sulforhodamine B dye, as described previously (1), and the viruses subsequently incubated with Alexa-488–labeled CR8020 IgG. Planar bilayers were formed in a microfluidic chamber on either dextran-functionalized glass coverslips (1) or PEG-functionalized glass coverslips where 5% of the PEG used was covalently coupled to the phospholipid 3-(*N*-succinimidyloxyglutaryl) aminopropyl, polyethyleneglycol-carbamyl distearoylphosphatidyl-ethanolamine (DSPE) (2, 3). Bilayer composition was supplemented with 1% molar fraction of the ganglioside Gd1a to allow virus immobilization. Upon pH drop, the viruses underwent full membrane fusion visualized as a loss of content dye from the viral lumen, indicating that a full fusion pore had formed (1). (*A*, *Top*) Increasing concentrations of CR8020 decreases the efficiency of full fusion (magenta squares). The hemifusion efficiency data (black)—aggregated from the data shown in Fig. 2*A* together with data previously reported (4) —is shown for comparison; full fusion shows a lower overall efficiency compared with hemifusion. (*A*, *Bottom*) Full fusion and hemifusion data were normalized to their respective efficiencies in the absence of CR8020. Best-fit lines using Eq. **S1** in Table S2 show good overlap between the two functional read outs and indicate that hemifusion inhibition is an appropriate read out for full fusion inhibition. (*B–D* and Movies S1–S3) Some viruses, which were bound by a subinhibitory number of CR8020 IgG molecules, showed outward diffusion of HA–CR8020 complexes into the DSPE–PEG-supported bilayer shortly after full fusion. Viruses were observed to fully disintegrate (*B* and Movie S1), partially disintegrate (*C* and Movie S2), or release only a small cluster of HA-CR8020 (*D* and Movie S3) following full fusion. The virus particle of interest is highlighted by a white, dashed box in *C* and *D*. In all images, SRB fluorescence from the viral lumen is colored in magenta, CR8020 fluorescence is colored in green, overlap between the two is seen as white. (Scale bars: 2 μm.) The first image of the montages ($t = 0$ or 1 s) demonstrate colocalization of the two fluorescence signals, and the full fusion event is marked with a magenta arrow in the second image ($t = 28$, 153, and 77 s, respectively). Subsequent montage images depict outward diffusion of HA in complex with CR8020. In *B* and Movie S1, labeling of the viral lumen by SRB was sufficient in this virus to allow visualization of the SRB molecules as they diffuse in the space between the glass coverslip and the tethered bilayer after full fusion. *B* and *C* include fluorescence trajectories from the virus particles of interest and show loss of the CR8020 fluorescence corresponding to full (*B* and Movie S1) or partial (*C* and Movie S2) disintegration of the viruses after the full fusion event. *D* shows an image montage from Movie S3 where, after full fusion ($t = 77$ s), a small HA–CR8020 cluster breaks off from the virus particle ($t = 191$ s, yellow square) and undergoes long-range, 2D diffusion. Below the image montage is the path of this small HA–CR8020 cluster overlaid on top of a maximum-intensity projection of Movie S3. The cluster's diffusional movement starts at the blue square near the virus particle on the lower right of the image and ends at the red square on the left. Note that for observing full fusion here, the bilayers were supported by PEG or dextran-functionalized coverslips to separate the lower bilayer leaflet (viewed from the side in Fig. 1*B*) from the glass surface. This design prevents interactions between the glass and the lipid bilayer, and creates an aqueous space for viral content release. When observing hemifusion, as in the main text, the lipid bilayer was formed on glass alone for experimental simplicity. This design was previously shown to provide equivalent kinetic hemifusion data (1) as fusion to a cushioned bilayer because the upper leaflet is equally fluid. In this latter experimental design, interaction between the bilayer lower leaflet and the glass prevents outward diffusion of both the GYPA and HA after fusion. As such, the HA–IgG signal does not disappear following hemifusion in our experimental design because the HA–IgG complex cannot diffuse away from the site of fusion.

1. Floyd DL, Ragains JR, Skehel JJ, Harrison SC, van Oijen AM (2008) Single-particle kinetics of influenza virus membrane fusion. *Proc Natl Acad Sci USA* 105(40):15382–15387.
2. Reich C, Andruzzi L (2010) Preparation of fluid tethered lipid bilayers on poly(ethylene glycol) by spin-coating. *Soft Matter* 6(3):493–500.
3. Mashaghi S, van Oijen AM (2014) A versatile approach to the generation of fluid supported lipid bilayers and its applications. *Biotechnol Bioeng* 111(10):2076–2081.
4. Brandenburg B, et al. (2013) Mechanisms of hemagglutinin targeted influenza virus neutralization. *PLoS ONE* 8(12):e80034.

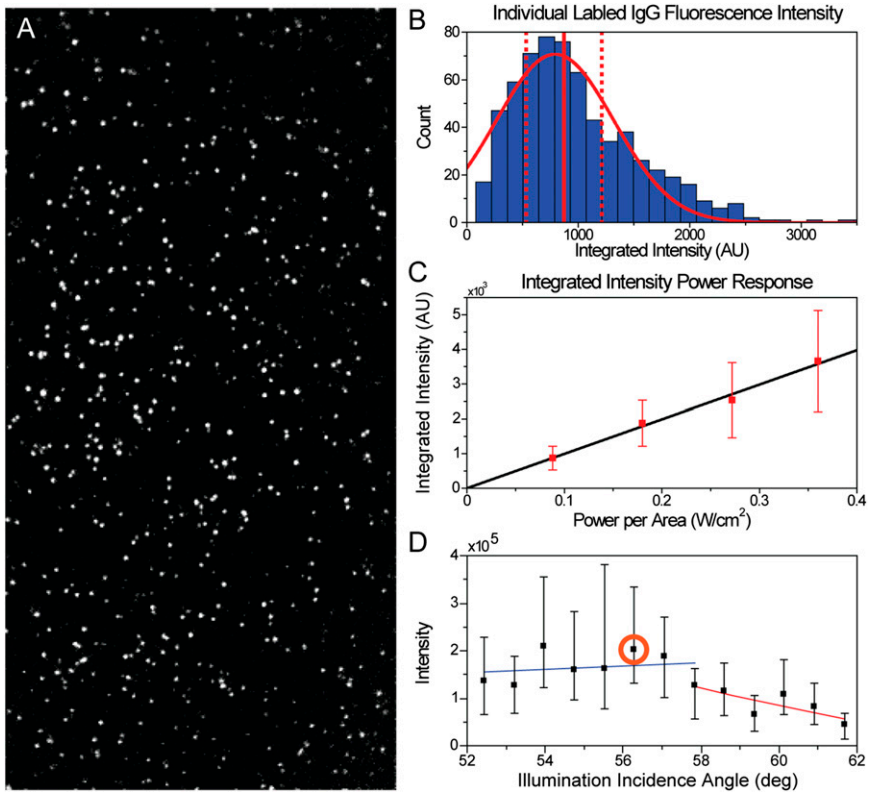

Fig. S5. Imaging of individual, labeled IgG molecules. (*A*) Representative image of CR8020af488-labeled IgG molecules adsorbed to a clean glass surface, visualized at ~0.1 W/cm^2 in pH 5.0 citric acid buffer, averaged over 100 frames acquired at 200 ms exposure time, and corrected for the Gaussian laser beam illumination profile. Image size is 512 × 256 pixels (140 × 70 μm). (*B*) Distribution of integrated fluorescence intensities acquired from *A*. The distribution is well fitted by a Gaussian distribution (red curve, $R^2 = 0.932$). The median value of this distribution (solid vertical line ± median absolute deviation, dashed lines) is taken as the integrated fluorescence intensity per IgG/Fab molecule used in calculating the number of bound IgG/Fab. (*C*) Median values of the averaged integrated fluorescence intensities, as measured in *B*, increases linearly with increasing laser illumination power, indicating that fluorescence read out of individual labeled IgG/Fab is linearly dependent on illumination input. (*D*) The angle of incidence of the excitation lasers upon the glass–water interface (horizontal axis) was varied to measure the fluorescence intensity (vertical axis) of CR8020af488 IgG bound to H3N2 virus incubated with 130 nM IgG and immobilized on a glass-supported bilayer. As expected, TIR occurred near 61° relative to the axis perpendicular to the glass surface. Data points are median values ± interquartile range. For angles smaller than 57°, the fluorescence intensity varied only slightly (blue line), indicating a homogenous evanescent field over the length scale of a virus. The effect of the evanescent wave was apparent for larger incidence angles (red line). The TIR angle was set to ~56° (orange circle) for all experiments to minimize the effect of the evanescent field but still achieve high signal-to-background recordings (*A* and Fig. 1*A*).

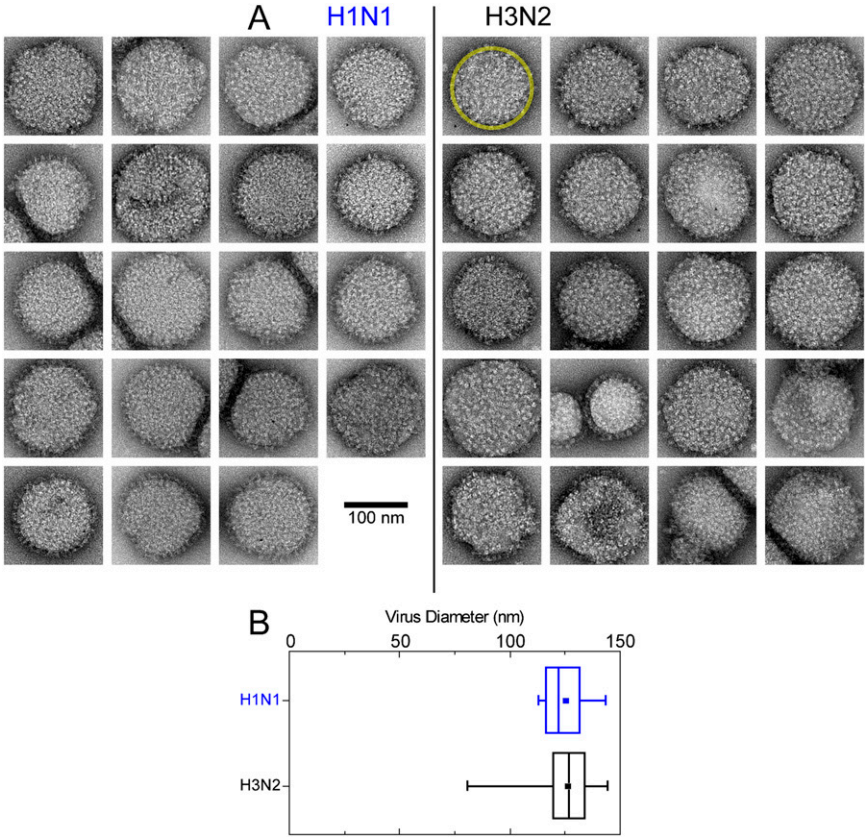

Fig. S6. Transmission EM of influenza strains H1N1 and H3N2. (*A*) H1N1 and H3N2 viral strains were diluted 1 million-fold to obtain nearly isolated particles and avoid deformation from virus–virus contact, then negatively stained with uranyl acetate on a carbon-coated TEM grid, and imaged at 45,000× magnification. In total, 19 of the 22 H1N1 viruses and 20 of the 26 H3N2 viruses imaged were used for diameter measurements. Both virus strains were spherical in appearance and generally had high surface spike protein density. Diameters of the virus particles were measured at the base of the spike proteins in the area of high contrast surrounding the virus, indicated by the yellow circle in the image. (*B*) Box plot of the diameters of the H1N1 (blue) and H3N2 (black). The square data point and vertical line inside the box represent the mean and median diameters, respectively. Left and right edges of the box are the 25th and 75th percentiles, respectively, and similarly the left and right whiskers are the first and 99th percentiles, respectively.

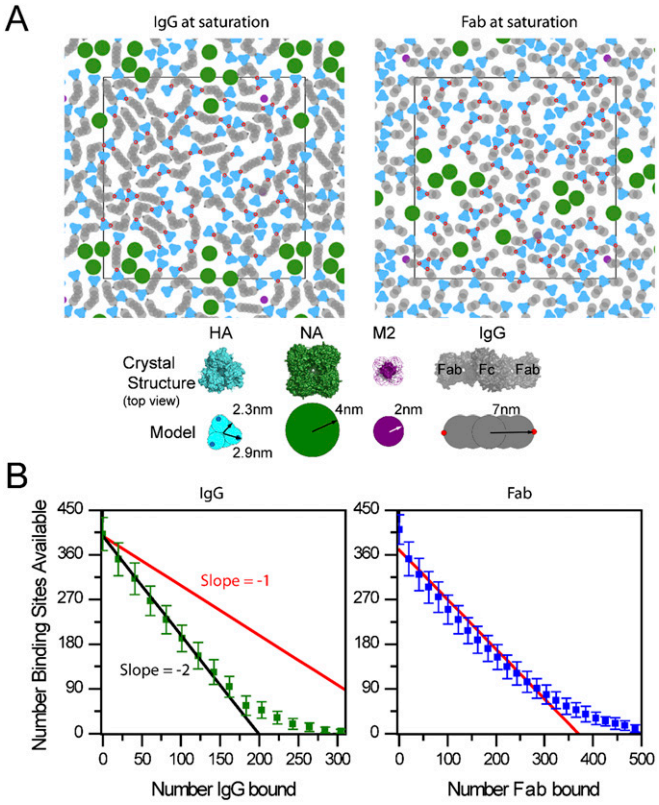

Fig. S7. Monte Carlo simulations of protein packing on a viral surface. (*A*) Simulated binding at full saturation when all binding sites are occupied by IgG (*Left*) or by Fab (*Right*). Simulations represented relevant proteins whose size corresponds to their crystallographic dimensions when viewed from the top, looking down on a viral surface. HA is in cyan, NA is in green, the M2 proton pump is in violet, and IgG (or Fab) is in gray. The spike protein (HA or NA) density shown corresponds to 8,000 spikes per square micron with a 7:1 ratio of HA:NA. Epitopes on the HA that are engaged with IgG or Fab paratopes are depicted as small, red circles. (*B*) The number of sterically available epitopes (vertical axis) diminished as the number of IgG (*Left*, green) or Fab (*Right*, blue) molecules on the viral surface increased. We see that no epitopes are sterically available when ∼270–300 IgG or ∼500 Fab molecules are bound. To approximate the rate of epitope loss upon IgG/Fab binding, lines having slopes of −2 (black) and −1 (red) are included. For IgG, the data closely follows the black line until ∼175 IgG are bound, suggesting that IgG binds with both paratopes to remove two binding sites up to this point. Beyond this region the rate of epitope loss deviates substantially from the black line (slope = −2), suggesting that each additional IgG does not bind with both paratopes. A majority of the Fab data are roughly parallel to the red line, as would be expected for single-paratope binding and low amounts of steric interactions, until more than ∼300 Fab had bound. We note that we have used only a single-spike density and HA:NA ratio leading to 375 total HA trimers on the viral surface, in accord with previous estimates for virus samples obtained through identical virus particle harvesting methods (1, 2). The polymorphic shape of other influenza viruses (not represented in our samples) could cause variation in the total number of HA present.

1. Harris A, et al. (2006) Influenza virus pleiomorphy characterized by cryoelectron tomography. *Proc Natl Acad Sci USA* 103(50):19123–19127.
2. Harris AK, et al. (2013) Structure and accessibility of HA trimers on intact 2009 H1N1 pandemic influenza virus to stem region-specific neutralizing antibodies. *Proc Natl Acad Sci USA* 110(12):4592–4597.

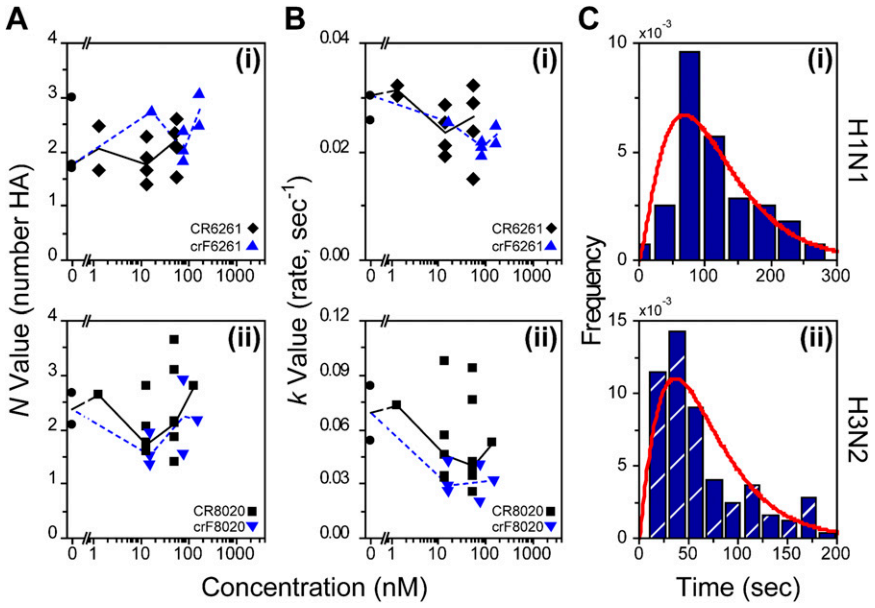

Fig. S8. Gamma distribution analysis of hemifusion times reveals a constant number of HA trimers needed for hemifusion at low and medium IgG/Fab coverage. (*Top*) Data is designated with *i* is for H1N1 bound by CR(F)6261 and (*Bottom*) *ii* is for H3N2 bound by CR(F)8020. Data points for IgG are in black and for Fab in blue; fit parameters in the absence of IgG/Fab are shown as circles in each plot. Median *N* (*A*) and *k* (*B*) values for each IgG or Fab concentration are connected by a solid black line or dashed blue line, respectively, and serve as a guide to visualize trends in the data. (*A*) The *N* parameter is interpreted to be the number of HA trimers participating in the membrane fusion process (1). Here we see that for both H1N1 (*A*, *i*) and H3N2 (*A*, *ii*), the number of HA required for fusion remains constant, between two and three, as IgG/Fab concentrations increase. This observation indicates that multiple HA are always required for hemifusion to occur. (*B*) The rate of the rate-limiting step in the fusion reaction is observed to decrease at higher IgG/Fab concentrations, in accord with data in Fig. 3. In addition, the H1N1 strain (*B*, *i*) is found to be slower than the H3N2 strain (*B*, *ii*), in agreement with Fig. 3. These kinetic behaviors are better demonstrated in Fig. 3 where all experimental data are shown, without a lower limit for number of events. (*C*) The hemifusion-time event-frequency distributions are shown for individual, representative experiments of H1N1 bound by crF6261 (*C*, *i*) and for H3N2 bound by crF8020 (*C*, *ii*) at concentrations of 160 nM Fab (blue) together with the corresponding gamma distribution fit curve (red). The rise-and-decay behavior is evident in the distribution even at this high Fab coverage, indicative of multiple kinetic steps being required for hemifusion to occur, as previously reported (1).

1. Floyd DL, Ragains JR, Skehel JJ, Harrison SC, van Oijen AM (2008) Single-particle kinetics of influenza virus membrane fusion. *Proc Natl Acad Sci USA* 105(40):15382–15387.

Table S1. Degree of IgG/Fab labeling and percent visualized

	Photobleaching		MALDI mass spectroscopy						
Fusion-inhibiting molecule	λ*	R^2	λ, $m/z = 1$*	R^2	λ, $m/z = 2$*	R^2	$\langle\lambda\rangle \pm$ SEM	Dyes per molecule ± SEM	Percent visualized†
CR6261	4.2 ± 0.1	0.950	6.87 ± 0.03	0.934	6.34 ± 0.03	0.959	6.6 ± 0.2	5.4 ± 0.8	99.5 ± 0.4
CR8020	4.3 ± 0.1	0.958	5.94 ± 0.02	0.955	5.29 ± 0.02	0.978	5.6 ± 0.2	5.0 ± 0.5	99.3 ± 0.3
crF6261	1.9 ± 0.2	0.850	2.73 ± 0.01	0.974	2.86 ± 0.02	0.941	2.80 ± 0.05	2.4 ± 0.3	91 ± 3
crF8020	2.1 ± 0.2	0.881	2.39 ± 0.01	0.964	2.56 ± 0.03	0.853	2.48 ± 0.06	2.3 ± 0.1	90 ± 1

*Results for Poisson distribution $[p(k,\lambda) = A \times (\lambda^k) \times \exp(-\lambda)/\Gamma(k+1)]$ fits from Fig. S3, where *A* was unconstrained to allow for various amplitudes; parameter errors are those reported by OriginLab plotting software during χ^2 minimization using mean residual variance and the parameter covariance matrix.
†Percent visualized corresponds to the percentage of labeled IgG/Fab molecules bound with at least one fluorophore. Error is calculated by error propagation for a Poisson distribution.

Table S2. Fit lines and corresponding estimated parameters determined by fitting data points from all experimental runs

Data and fit model	Parameter	H1N1 CR6261	H1N1 crF6261	H3N2 CR8020	H3N2 crF8020
Hemifusion efficiency [$E(c)$]	A	0.006 (−0.009, 0.021)	0.011 (−0.001, 0.023)	0.033 (−0.005, 0.072)	0.033 (0.017, 0.049)
$\text{logit}[E(c)] = \text{logit}\left[D + \frac{A-D}{1+\left(\frac{c}{10^{C_0}}\right)^p}\right]$ **[S1]***	C_0	1.777 (1.275, 2.279)	2.151 (1.906, 2.397)	2.108 (1.861, 2.356)	1.894 (1.726, 2.063)
	D	0.472 (0.302, 0.641)	0.454 (0.326, 0.582)	0.590 (0.502, 0.679)	0.603 (0.490, 0.716)
	p	−1.078 (−1.629, 0.527)	−2.232 (−3.755, −0.708)	−1.324 (−1.904, −0.744)	−2.245 (−3.460, −1.030)
No. of molecules bound [$N(c)$]	M	175.3 (121.5, 229.1)	248.1 (158.1, 338.1)	144.4 (119.1, 169.6)	492.5 (393.5, 591.6)
$\sqrt{N(c)} = \sqrt{\frac{M \times c}{10^z + c}}$ **[S2]**	z	2.514 (2.178, 2.849)	2.525 (2.162, 2.887)	1.959 (1.731, 2.187)	1.843 (1.576, 2.111)
	t_0	1.660 (1.546, 1.773)	1.704 (1.531, 1.877)	1.421 (1.318, 1.524)	1.466 (1.416, 1.515)
Time to hemifusion [$t(c)$]	B	0.339 (0.207, 0.470)	0.433 (0.212, 0.655)	0.326 (0.184, 0.468)	0.414 (0.353, 0.478)
$t(c) = t_0 + \frac{B \times c}{10^{C_1} + c}$ **[S3]**†	C_1	1.461 (0.861, 2.060)	1.937 (0.985, 2.889)	1.982 (1.229, 2.736)	1.657 (1.415, 1.898)

Values in parenthesis represent 95% confidence bounds (lower, upper). For stabilization of all models, the hemifusion data without IgG were placed at an infinite low IgG concentration. All statistical analysis for fitting was performed using proc NLMIXED (SAS Version 9.2). Where necessary (Eq. **S1**), fitting involved a restriction that the lower asymptote was ≥ 0. Standard errors and 95% confidence limits were estimated using the delta method (1, 2). Eq. **S1**: E represents the proportion fusion events over total events, D and A represent respectively the upper and lower asymptote, p represents a slope factor, C represents the IgG/Fab concentration (in nanomolars) and C_0 represents the inflection point. Eq. **S2**: N represents the number of bound IgG/Fab defined as (median intensity)/(labeling correction × intensity per molecule), C is the concentration of IgG/Fab (in nanomolars), M is the maximum number of IgG/Fab that can bind and Z is the IgG/Fab concentration where the half-maximum number of molecules bind. Eq. **S3**: t represents the time to hemifusion, t_0 the time to hemifusion without IgG/Fab, B the interval between t_0 and the upper asymptote, C represents the IgG/Fab concentration (in nanomolars) and C_1 represents the IgG/Fab concentration corresponding to the geometric mean of t_0 and B being modeled on a $\log_{10}$ scale.

*Confidence intervals for 50% hemifusion efficiency reduction reported in Table 1 and *Results* were calculated using the delta method (1, 2) and the lowest degrees of freedom from the two models.

†Parameters B, C_1, and t_0 were modeled on a $\log_{10}$ scale.

1. Billingsley P (1986) *Probability and Measure* (John Wiley & Sons, Inc., New York).
2. Cox C (1998) *Encyclopedia of Biostatistics*, eds Armitage P, Colton T (John Wiley, New York), pp 1125–1127.

Movie S1. Complete virus disintegration. Full virus disintegration allowing outward diffusion of all HA–CR8020 complexes into the DSPE–PEG-supported bilayer shortly after full fusion. Labeling of the viral lumen by SRB was sufficient in this virus to allow visualization of the SRB molecules as they diffuse in the space between the glass coverslip and the tethered bilayer after full fusion. SRB fluorescence from the viral lumen is colored in magenta, CR8020 fluorescence is colored in green, overlap between the two is seen as white. (Scale bars, 2 μm.) The full fusion event is indicated with a magenta arrow and HA–CR8020 diffusion is indicated by green arrows.

Movie S1

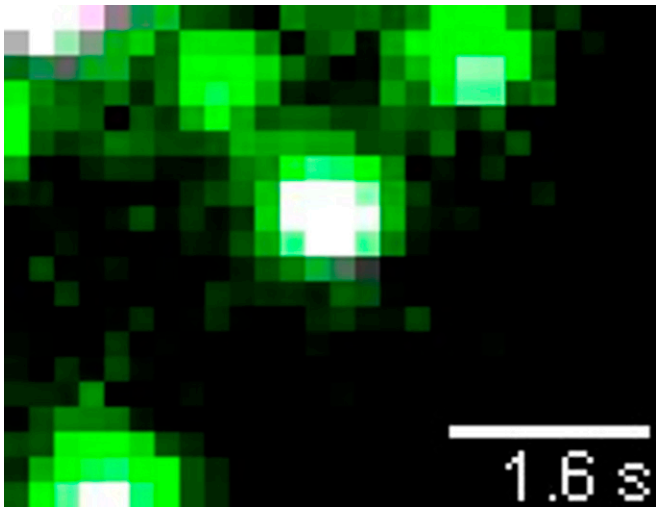

Movie S2. Partial virus disintegration. Partial virus disintegration allowing a portion of the HA–CR8020 complexes to diffuse outward into the DSPE–PEG-supported bilayer shortly after full fusion. The portion of HA–CR8020 observed to break off from the main virus particle is seen to itself disintegrate, with smaller HA–CR8020 clusters diffusing outward. SRB fluorescence from the viral lumen is colored in magenta, CR8020 fluorescence is colored in green, overlap between the two is seen as white. (Scale bars, 2 μm.) The full fusion event is indicated with a magenta arrow and the main HA–CR8020 diffusion event is indicated by green arrows.

Movie S2

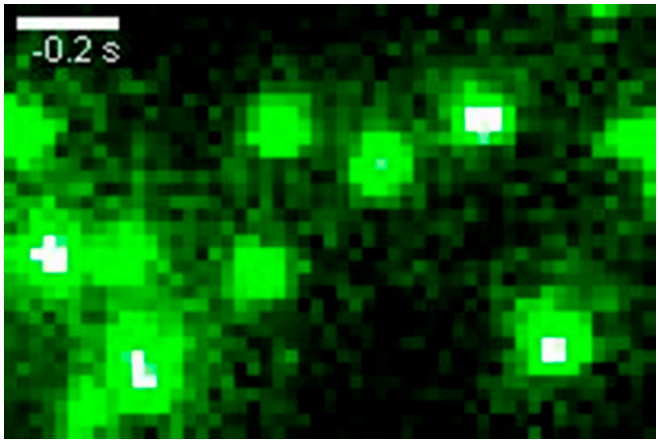

Movie S3. Long diffusion of small HA-CR8020 cluster. Release of a small cluster of HA–CR8020 complexes into the DSPE–PEG-supported bilayer after full fusion occurs. The cluster stays together for a substantial amount of time and undergoes long-range, 2D diffusion. SRB fluorescence from the viral lumen is colored in magenta, CR8020 fluorescence is colored in green, overlap between the two is seen as white. (Scale bars, 2 μm.) The full fusion event is indicated with a magenta arrow and the initial portion of the HA–CR8020 diffusion trajectory is indicated by green arrows.

Movie S3